Summer 2019

Mechanical Characterization and Non-Destructive Evaluation of SiC_f/SiC_m Composites for Nuclear Applications

Donald J. McCleeary

MECHANICAL CHARACTERIZATION AND NON-DESTRUCTIVE EVALUATION OF SiC_F/SiC_M COMPOSITES FOR NUCLEAR APPLICATIONS

by

Donald J. McCleeary

Bachelor of Science
University of South Carolina, 2015

Submitted in Partial Fulfillment of the Requirements

For the Degree of Master of Science in

Mechanical Engineering

College of Engineering and Computing

University of South Carolina

2019

Accepted by:

Xinyu Huang, Director of Thesis

Jingjing Bao, Reader

Cheryl L. Addy, Vice Provost and Dean of the Graduate School

DEDICATION

Written words, the most powerful tools of human expression, cannot adequately dedicate this work to the many family, friends, and teachers that have graciously provided their support and experience to the completion of this achievement.

To all of you, thank you

ACKNOWLEDGEMENTS

My advisor Dr. Xinyu Huang deserves the utmost credit, for without his extensive knowledge, support, and ever-enduring patience none of this would be possible. Special thanks also go to my mentors Dr. Jingjing Bao, Dr. Myoungseok Lee and Dr. Luis Alva who provided useful assistance and lengthy instruction in matters of which I was ignorant. Also, to my current and former peers in the lab, best wishes to you and your careers. Thanks to General Atomics, specifically Dr. Hesham Khalifa and Dr. George Jacobsen who provided critical materials, resources and collaboration in support of these projects. Finally, thanks to my family, specifically my loving wife Kristie who has loudly supported my endeavors, my parents Brad and Donna for pushing me to succeed, and my late grandfather Don Snider who taught me the joy of hard work and success.

This work was performed at the University of South Carolina, Mechanical Engineering Department, in collaboration with General Atomics. Funding was provided by the Department of Energy Office of Nuclear Energy under the Accident Tolerant Fuel Program, DE-NE0000566 and DE-NE0008222. This report was prepared as an account of work partially sponsored by an agency of the United States Government. Neither the United States Government nor any agency thereof nor any of their employees make any warranty, express or implied, or assumes any legal liability or responsibility for the accuracy, completeness, or usefulness of any information, apparatus, product, or process disclosed, or represents that its use would not infringe privately owned right.

Reference herein to any specific commercial product, process, or service by trade name, trademark, manufacturer, or otherwise does not constitute or imply its endorsement, recommendation, or favoring by the United States Government or any agency thereof. The views and opinions of the authors expressed herein do not necessarily state or reflect those of the United States Government or any agency thereof.

ABSTRACT

The SiC_f/SiC_m composite material is a promising candidate for accident tolerant fuel cladding in light water reactors and for structural elements in high temperature reactors. The material demonstrates exceptional toughness when compared to monolithic ceramics. It is critical to characterize the mechanical behavior, internal damage and ultimate strength of these composites under relevant loading conditions. In this thesis, the author developed and improved several mechanical characterization and non-destructive evaluation methods and applied them to SiC_f/SiC_m composites. Impulse excitation (IE) analysis of damaged SiC_f/SiC_m composite disks following controlled impact testing shows a direct relationship between the damage applied to SiC_f/SiC_m composite disks and changes in the flexural and torsional resonant frequencies of the disks, as well as a proportional relationship between the change in frequencies and energy absorbed. An experimental exploration of the "size effect" of SiC_f/SiC_m composite tubes shows a relationship between the length of the material and its burst strength. Samples consistently showed a UTS increase of as much as 33% between samples of approximately 15cm lengths and those of 28cm lengths following repeated burst testing, though further testing is required to fully understand the reasons for this reduction. In the context of SiC_f/SiC_m composites, novel DIC setups are discussed which are improvements over traditional setups and have a higher capability of capturing the full field strain map of tubular objectives. First, a 3D DIC setup

using one camera and mirror splitting is tested and compared with a traditional DIC two-camera setup, showing comparable results along with a host of extrinsic benefits. Lastly, the mirror splitting concept is taken a step further in an exploration that uses a six-mirror setup and telecentric lens to realize 360˚ surround views for the purpose of capturing the failure sites.

TABLE OF CONTENTS

LIST OF TABLES

LIST OF FIGURES

LIST OF ABBREVIATIONS

AE ..... Acoustic Emission

ASTM ..... American Society for Testing and Materials

ATF ..... Accident Tolerant Fuel(s)

BCC..... Body Centered Cubic

CVI ..... Chemical Vapor Infiltration

DAQ ..... Data Acquisition

DIC ..... Digital Image Correlation

DOE ..... Department of Energy

DWIT ..... Drop Weight Impact Tower

ECCS ..... Emergency Core Cooling System

FCC ..... Face Centered Cubic

FFT ..... Fast Fourier Transform

IE ..... Impulse Excitation

LOCA ..... Loss-Of-Coolant Accident

LWR ..... Light Water Reactor

NDE ..... Non-Destructive Evaluation

NITE ..... Nano-Infiltration Transient Eutectic

ORNL ..... Oak Ridge National Laboratory

PLS ..... Proportional Limit Strain

RFDA ..... Resonant Frequency and Damping Analyzer

SiC .....Silicon Carbide

SiC_f/SiC_m .....Silicon Carbide Fiber/ Silicon Carbide Matrix Composite

TEP .....Transient Eutectic Phase

UTS ..... Ultimate Tensile Stress

CHAPTER 1
INTRODUCTION AND LITERATURE REVIEW

1.1 BACKGROUND

On March 11, 2011 a tsunami hit the coast of eastern Japan, causing a disruption in coolant flow to the reactors located at the Fukushima Daiichi power plant. The accident itself as well as the resulting release of radiation to the environment raised serious safety concerns regarding the use of Zr fuel claddings. Shortly after the disaster occurred, the United States Congress directed the Department of Energy (DOE) to focus efforts on the research and implementation of fuels which could prevent core meltdown in the event of a loss of coolant accident (LOCA). In response, the DOE started the Accident Tolerant Fuel (ATF) program and began to gather talent and research attention to the issue by organizing and channeling financial resources into industrial partners and universities [1]. The effect of this action has produced an intense focus on ATF and since 2011 an expansive amount of research has been completed on the subject.

In an exhaustive summary of the progress made in ATF since Congressional action, Terrani [2] provides an extensive overview the three most actively pursued claddings, their development, and the critical challenges that still must be overcome in each respective field. His summary also includes the design philosophy of ATF cladding as well as important information regarding the evolution and properties desirable to ATF. Much of

the information that was used in that review, including citations, are referenced in this introduction.

Figure 1.1: Fukushima Daiichi reactors 1-4 (right to left) following the March 11 Tsunami [3]

Still, a great deal of work remains to be completed for the short-term and long-term plans for the implementation of ATF. In the nuclear industry a culture of safety, careful examination and detailed analysis leads to slow change and implementation of new ideas. Despite this, the DOE has demanded results by 2022, when they expect commercialization of ATF into existing light water reactor (LWR) systems to begin. Since 2012, the DOE has primarily sponsored several leading nuclear developers, including Framatome, General Electric, and Westinghouse Electric, each charged with developing a different set of ATF fuels and claddings [4].

1.2 THE PROBLEM

The primary goal of ATF is the reduction of cladding oxidation in the event of an accident. When Zr cladding comes into contact with hot steam in a LOCA scenario, it reacts exothermally to produce zirconia and hydrogen, which in the case of Fukushima resulted in the explosions of reactor units 1, 2 and 3. This exothermic reaction is provided in *Equation 1* with the thermal energy product Q boldened for clarity. Needless to say, the presence of hydrogen gas in an accident greatly compounds the severity and was a large part of the terrible nature of the Fukushima Daiichi event. This reaction has a substantial effect on the forecasted temperature of the system as well, as is shown in *Figure 1.2*, driving the temperatures of the system to climb very high after initiation of the accident and remain so for many days. If this reaction can be minimized or eliminated from the system, the effect would be a substantial reduction in the temperature increase rate and maximum temperature. This reduces, to a certain extent, the severity of a crisis while also relieving a great deal of the burden placed on the emergency core cooling system (ECCS). *Figure 1.2* displays a graph of the heat added to the reactor system following a shutdown.

The main forms of cladding under consideration are coated Zr claddings, iron-chrome-aluminum (FeCrAl) claddings, and silicon carbide fiber/ silicon carbide matrix composite claddings ($SiC_f/SiC_{m)}$. Westinghouse and Framatome are the industrial developers responsible for the most part in research dealing with chrome coated zirconium. As a cladding, it represents perhaps the easiest and most well understood cladding material currently under research, due to the fact that the addition of a chromium layer to traditional Zr claddings does not change the core mechanical behavior of the fuel. However, there are still major design problems with this material. The most significant challenge associated

with chrome coated Zr is that for a coolant-limited accident the rods can balloon and burst at as low as 700˚C [5], effectively circumventing the chrome coating and exposing the interior of the rod to oxidation. Also, Zr as a material is approaching its performance limit within LWRs and is currently being phased out or eliminated entirely in future designs.

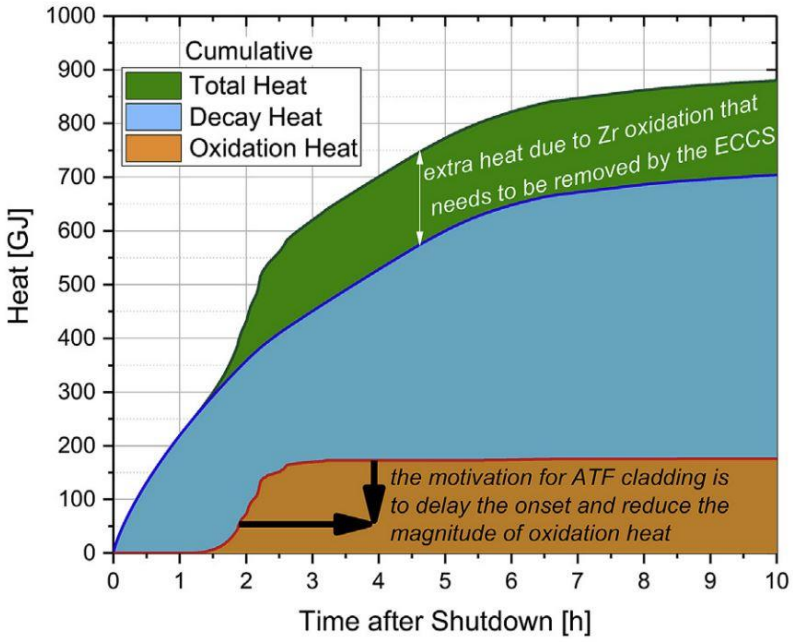

Figure 1.2: LWR Heat/Time after Shutdown [2]

$$Zr + 2H_2O \rightarrow ZrO_2 + 2H_2 + Q\ (140\frac{kcal}{mole}[6]) \qquad \textit{(Eqn 1)}$$

FeCrAl cladding is being developed by Oak Ridge National Laboratory (ORNL) and General Electric and shows promising steam oxidation resistance up to its melting point at approximately 1500˚C [7,8,9]. Austenitic Fe based claddings were the original cladding used in the inception of nuclear power in the 1950's, but were quickly replaced

with Zr claddings because they were prone to react with the oxygen-rich coolants that were used prior to the 1990's, producing extreme cases of stress corrosion cracking. However, changes to the crystal structure of Fe from face centered cubic (FCC) to body centered cubic (BCC) have since shown to improve this performance problem [10], and the addition of at least 22 wt% Cr content promotes the formation of protective chromia films [11,12]. However, the natural neutron absorption of Cr and Fe within these claddings is much higher than that of Zr [13]. Also, BCC Fe alloys tend to allow tritium to escape from the fuel and pass through the cladding walls. Its tritium permeability is two orders of magnitude higher than Zr claddings [14].

1.3 SiC_F/SiC_M COMPOSITE CLADDING AS A SOLUTION

Silicon carbide (SiC) is one of the hardest materials known to man but is also very brittle, which can create catastrophic failures under accidental conditions. It was found that SiC fibers embedded in a matrix of monolithic SiC (SiC_f/SiC_m) could overcome this problem by allowing the material to fail "gracefully" [15]. Judging by stress/strain curves, this very effectively increases the strain-to-failure and adds a great deal of energy dissipation during the failure process. Today, the use of SiC composites are rapidly growing in aerospace industry because of their ability to maintain high strength, toughness, rigidity, and creep resistance at high temperature.

All of the aforementioned qualities that make SiC_f/SiC_m composites ideal for work in the aerospace industry would also make them suitable for use as cladding materials in nuclear reactors. Therefore Westinghouse, in collaboration with General Atomics, was charged by the DOE with developing SiC composite cladding for implementation. Compared to other materials considered for use in ATF, SiC provides the most exceptional

oxidation resistance in steam, and for this reason SiC_f/SiC_m composite claddings made from Generation III SiC fibers with chemical vapor infiltration (CVI) or nano-infiltration transient eutectic phase (NITE) have been referred to as the ideal ATF cladding material [2]. Add to this acceptable performance under neutron irradiation [16] and one would seem to have a perfect solution to ATF.

Figure 1.3: SiC_f/SiC_m composite turbine blade [17]

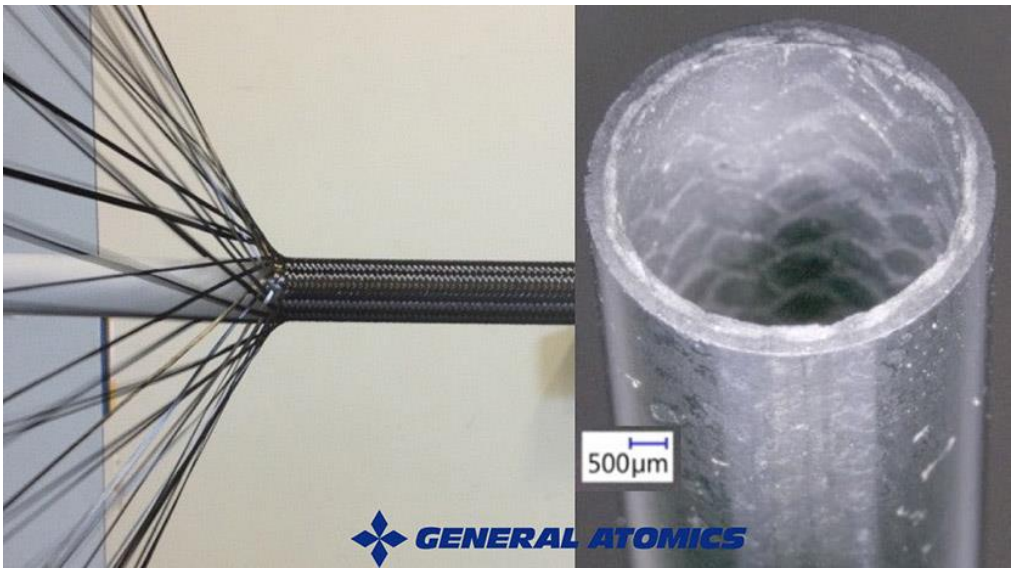

Figure 1.4: General Atomics SiC_f/SiC_m composite cladding winding process and material [18]

However, SiC_f/SiC_m composites are not without challenges. The primary concern with this material lies with the brittle nature of the matrix material. While the fiber reinforcement does an excellent job of preventing catastrophic failure, damage to the matrix itself in the form of cracks or even microcracks open pathways for radionuclide release and develop a failure mode that is unique to SiC fuel cladding. Matrix cracking can occur in SiC cladding due to mechanical stress applied to the cladding itself or as a result of the temperature gradient and neutron irradiation that the cladding experiences [2]. Furthermore, SiC cladding encounters a particular manufacturing issue when it comes to fabricating end plugs for the clad. Katoh et. al. [19] cite these two mechanical issues as some of the key problems facing SiC cladding, though since then General Atomics has developed a method to seal the ends of SiC cladding with a "high-purity SiC joint that maintains strength and hermeticity at high temperatures" [18].

Terrani [2] focuses on reiterating the potential for radionuclide release as a cause for major concern. He suggests that this may be overcome by adding a protective metal layer of some kind which would prevent radionuclide release in the likely event of matrix cracking. The protective barrier would also protect the cladding from another weakness of SiC: corrosion in the presence of high temperature, high pressure water, which he calls hydrothermal corrosion, that occurs as SiC reacts with O in the coolant water to produce soluble silica, as well as CO, CO_2, and CH_4.

1.4 MECHANICAL CHARACTERIZATION

As can be guessed from the aforementioned details regarding ATF claddings, before commercial production and implementation of the material begins every detail of these fuels must be studied, characterized, modelled and optimized for use in real reactor systems. A significant piece of the puzzle is mechanical characterization and behavior analysis of the cladding material. By simulating stress states and environmental conditions, experimentation on the cladding is the only way to grasp how the material will actually perform under relevant loading conditions. Furthermore, models used to predict this behavior rely on experimental data for validation, leading to verified models that can be confidently relied on to provide useful projections. Many experiments have been devised to qualify the behavior of cladding materials under expected and accidental LWR conditions, including tensile, torsion, internal pressure, external pressure, drop weight impact, Charpy impact, creep, quench, and extended vibration tests. Furthermore, many combinations of these loading conditions have been implemented to characterize the cladding mechanical behavior.

In this work, two important material behaviors are discussed and experiments carried out in the context of SiC_f/SiC_m composites. The first is referenced in Chapter 2 and discusses impulse excitation (IE) analysis of damaged SiC_f/SiC_m composite disks. Three as-fabricated SiC_f/SiC_m composite disks of similar geometry were impacted in order to induce a controlled amount of damage to each specimen. After each test IE results were collected and tabulated in order to gauge whether there is a change in the flexural and torsional frequencies and damping. The results of impact testing are displayed as well as IE change across each test.

The second facet tested in this work is that of mechanical behavior of SiC tubes under internal loading conditions and of a size effect that may be present within the material. This is thought of to be due to the probability of manufacturing defects residing within the material and is manifested by an increase in material strength as the sample becomes shorter. Burst tests were conducted to find evidence of a size effect and to attempt to quantify it, the results of which can be found in Chapter 3. Three tubular samples of geometries resembling cladding material were burst using a hydraulic internal pressurization method. Typically, when SiC_f/SiC_m composite tubes are burst in this manner, a short hinging crack develops across a small portion of the tube. In this study, these portions were then removed from the sample by cutting with a diamond blade and were then used as more test specimens. Testing samples in this manner can provide clues as to whether a size effect exists.

1.5 DIGITAL IMAGE CORRELATION

SiC composites are inherently anisotropic and do not exhibit uniform strain within the material under load. This greatly complicates testing, data analysis, and modelling of

the material behavior and can lead to an incorrect analysis if the cladding strain is not properly mapped. Digital image correlation (DIC) is an excellent tool with which a portion of the strain field on the outer surface of a test specimen can be viewed and quantified. DIC was originally proposed for this purpose by Sutton et. al. [20] in 1985 and since that time has become a widely used and trusted technique in industry and academia to observe strain patterns in materials. Using this technology for the research of SiC_f/SiC_m composites is a logical step in understanding the matrix-fiber interaction during failure.

Even so, work still needs to be done to improve this measurement tool. One primary problem with DIC is that it only views a small area of the surface of a specimen, when in the context of SiC composites this may be a deficient practice as it can be difficult to predict where failure may occur. This problem can be mitigated with the use of multiple cameras and DIC setups, but this becomes further complicated with time consuming setup, the multiplied cost of having multiple cameras, data buffers that are too small, synchronization errors, and error in DIC results caused by differences in sensitivity between cameras.

In Chapter 4 of this work, two novel setups are described which can alleviate these problems using optics designed for single optics. The first setup is for a 3D DIC system using a single camera which was first suggested by Inaba et. al. [21]. This setup cuts the necessary number of cameras in half while reducing sensitivity error and eliminating entirely problems with camera orientation, data buffering, and synchronization problems when only one view of the specimen is required. The second setup is similar to the first but takes the design a step further by introducing a large telecentric lens and two rear-view mirrors. The purpose of this design is to capture a 360 degree surrounding view of a tubular

sample (such as nuclear fuel cladding) in order to capture imagery of the site of failure and measure strain using 2D DIC.

CHAPTER 2

IMPACT TESTING AND IMPULSE EXCITATION RESPONSE OF SiC_F/SiC_{FM} COMPOSITE DISKS

2.1: INTRODUCTION

Since SiC_f/SiC_m composites are quite new to researchers, there exists a need to discover simple nondestructive evaluation (NDE) methods by which SiC composites can be tested to gauge damage within the material [22]. Unnthorsson et. al. [23] describe the three stages of life of composite materials, and damage effects that can be encountered within those stages. The first stage begins with the manufacturing of each component and reveals the very real possibility that composites can begin to accrue damage even before assembly. This work is discussed more later in this thesis in the context of size effect, but here it shows the sensitivity in quality of composite materials.

For brittle isotropic specimens, impact damage is typically associated with failure and is usually simple to determine by visual inspection. This is because most of the energy that would occur during an impact is deflected back to the impactor or otherwise removed from the sample via other forms of energy such as vibration or sound. It is only when the amount of impact energy passes a certain threshold (e.g. stress leading to response in excess of proportional limit strain) that the sample begins to absorb more energy and the material structure is changed as a result. In this case, structures will deform, crack, or rip, essentially accruing damage and failing at the same time.

In contrast, SiC composites can accrue damage without failing catastrophically. Once past the loading threshold for damage to occur, the SiC composite specimen can fail locally in a variety of ways, namely matrix cracking, interfacial debonding, delamination, and tow breakage [24,25]. However, the local occurrence of damage may not necessarily lead to failure of the entire specimen. If catastrophic failure occurs, it is largely related to the performance of the fiber-matrix interface. What complicates this is that the acquisition of damage by the sample may not be simple to determine. Much of the energy absorbed as damage in a SiC_f/SiC_m composite occurs within the body of the structure as opposed to being visible on the surface [26]. Also, the full nature of the damage may not be readily visible or appreciable under X-ray tomography [27] or ultrasonic analysis [28]. Truesdale [29] lists nine NDE techniques and cites many disadvantages to NDE methods, which include limits in material use, limitations in sample geometries, complex or expensive setups and extensive calibration requirements. Furthermore, none of these methods provide a swift and easy means by which damage in the specimen may be quantified. Acoustic Emission (AE) as an NDE method can provide a better description of damage, but a disadvantage of AE is that it cannot be collected after a sample has accrued damage and must be active during the entirety of the damage event. Also, AE NDE is further limited to analysis of the energy due to acoustic release of damage and may not be indicative of all energy absorbed as damage by the specimen.

IE is a nondestructive technique through which delicate changes in a material can be discovered by impulsing or applying a small impact to the specimen [30]. When supported freely and suspended along nodal lines, every specimen will react to excitation by invoking a harmonic response. This response has several modes and unique modal

frequencies which are dependent on the material properties and geometry of the specimen and can be analyzed by passing the signal through a fast Fourier transform (FFT) to deduce the major frequencies. Because of this, important material properties can be deduced from the associated frequencies, such as elastic modulus, shear modulus, and Poisson's ratio [30,31], though this is always discussed in traditionally accepted literature from the context of isotropic materials. However, it is worth noting that research performed at ORNL shows promising results in using IE to accurately measure the material properties of SiC_f/SiC_m composite bars [32], and that Truesdale further explores this idea in the context of cladding geometries and finds Young's modulus and shear modulus within acceptable error [29]. Truesdale also points out that IE provides limited damage categorization. While this is true in that specific types of damage (pre-existing or otherwise) are difficult to determine using IE alone, it is important to note that the shift of IE response indicates a change of the status of the material, even though the specific location and form of the material change (damage) may be difficult to interpret in detail using IE alone. This technology is also intuitive and has been implemented in damage detection for over 100 years, dating at least as far back as the early implementation of trains and railroads when service personnel called modal specialists would test each train wheel with a hammer and listen for variations in the response [33].

In the case of fiber/matrix composites the material property data becomes unclear, but the resonant frequencies produced are still dependent on material geometry. As such, it stands to reason that as a fiber/matrix composite absorbs energy in the form of damage, those frequencies should change as well [34]. Truesdale discovered a direct correlation between the shift of harmonic frequencies produced by a tubular SiC_f/SiC_m specimen and

damage it had accrued in the process of various loading programs. As damage was induced on the composite claddings, the frequencies became lower and the dampings of each mode became higher. If IE is to be used for damage detection, it would be useful to find ways to connect change in frequency and damping to quantitative measures of damage. One quantitative measure of damage may be total energy absorbed over the course of damage, but assuming that the change in frequency of a sample is somehow correlated to energy absorbed, it would require controlled examination to establish a trend. To gather results from such an experiment, a drop weight impact tower (DWIT) was used to impact multilayered SiC_f/SiC_m composite disks under controlled conditions and record the energy absorbed, and IE instrumentation was used in accordance with American Society for Testing and Materials (ASTM) standards to measure the frequency response prior to the controlled impact.

2.2 THE SiC_f/SiC_m FLAT DISKS

Three samples, here labelled disks 1, 2 and 3, were provided by General Atomics for testing. Each were of similar flat disk design, measuring approximately 50mm in diameter by 3mm in thickness. These disks were made up of a β-phase monolithic SiC matrix sandwiched around multiple laminae of woven SiC fibers and were manufactured using transient eutectic phase (TEP) processing via hot pressing. It is important to note that the TEP process is noticeably different than the CVI process in that a hot press is used for powder compaction. Each sample was lightly polished by the manufacturer to remove surface roughness.

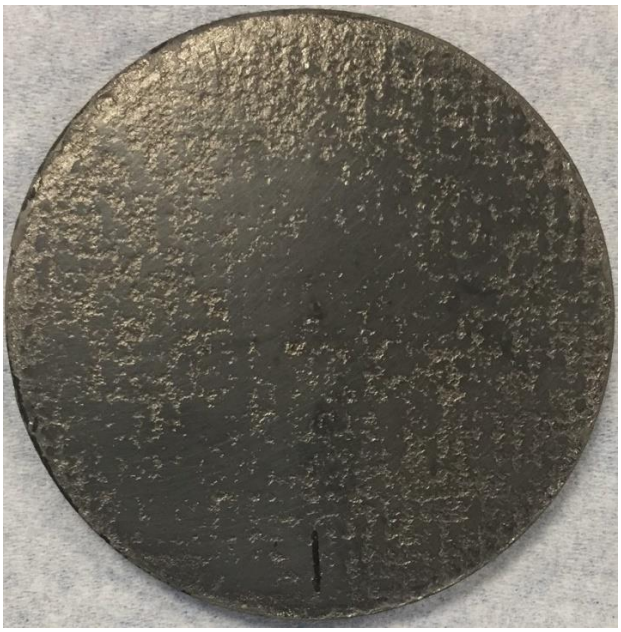

Figure 2.1: Pristine SiC_f/SiC_m Disk (Disk 1), mark on bottom added to indicate orientation and impact side.

2.3 IMPULSE EXCITATION

The system used to measure the impulse excitation response of the SiC_f/SiC_m disks was an IMCE resonant frequency and damping analyzer (RFDA) IE suite designed for measuring material properties according to ASTM standards E1875 [35] and E1876 [36]. The system consists of a sample scaffold, a microphone, and computational tools used in the collection, measurement, and recording of high frequency material responses.

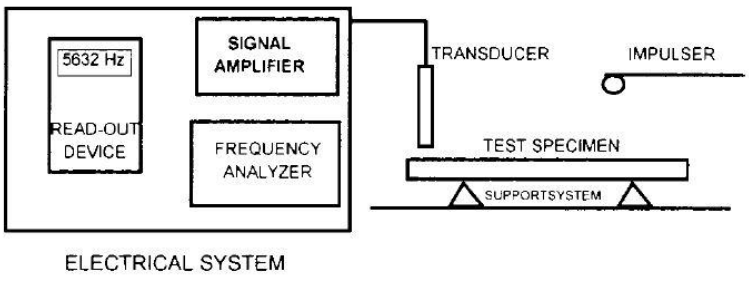

Figure 2.2: IE System Diagram [36]

The material in question was suspended on a set of wires along the nodal lines of the material to prevent the wires from interfering with the response of the material. Then, the material was quickly struck by an impulsor with low force in order to excite a harmonic response from the material. This response, subdivided into torsional and flexural vibration modes, was picked up and recorded by the sensitive microphone. Two properties of the resonant vibration modes were recorded: The resonant frequency and the damping of the signal. The specific frequencies produced are inherent to the geometry and consistency of the matter making up the specimen, and so are the damping ratios which represent the vibrational losses of the material [37].

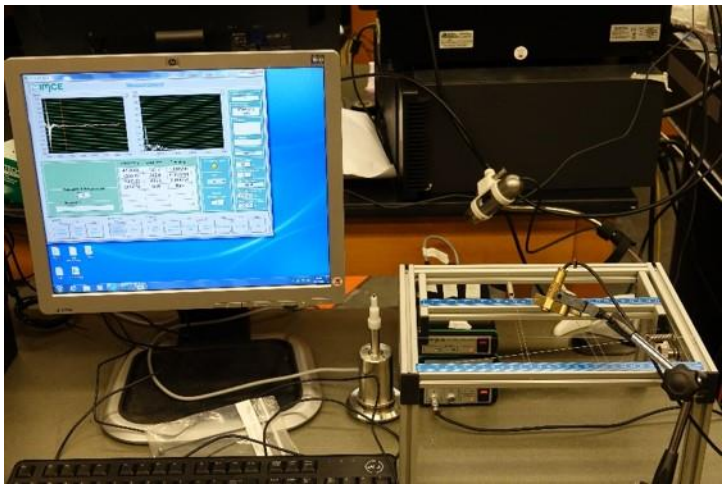

Figure 2.3: IE setup

Flat disks can vibrate in various flexural and torsional modes. Torsional vibration can be thought of as a wave emanating from the center of the disk and stretching out to the edges of the disk, always remaining concentric with the center. Flexural vibration occurs in four quadrants of the disk and its motion behavior is represented by nodal and antinodal lines. The nodal lines represent the points of minimum or zero vibrational displacement

whereas the antinodal lines represent the maxima. Samples are aligned on two perpendicular suspension cables of small thickness so as to match the nodal lines as closely as possible and prevent the line from interfering with signals generated by the impulse. *Figure 2.4* displays the concept of the anti-flexural nodal and antinodal lines on disks.

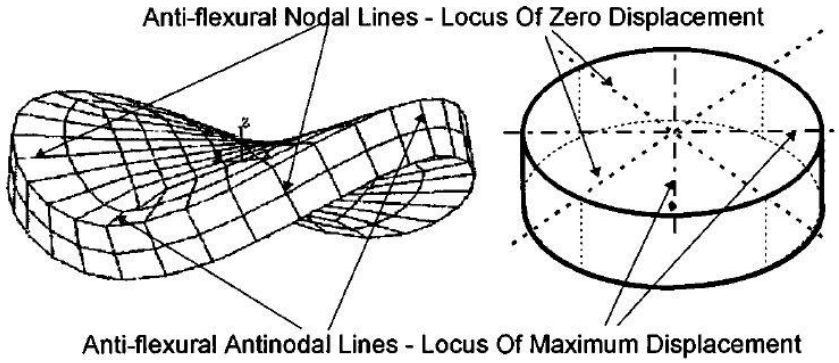

Figure 2.4: Display of antiflexural nodal and antinodal lines on flat disks [36]

This measurement followed ASTM E1876 [36]. The samples were positioned on the setup as previously discussed and a microphone was positioned at the antinodal intersection opposite of the point of the impulse. Each impulse was performed manually using an impulsor, a steel ball attached to a flexible polymer rod, at the position indicated by the diamond shape in *Figure 2.5*. Care was taken to use approximately the same amount of force with each impact, but this has little effect on the frequencies and damping signal produced as it is material dependent, and independent of the amplification of the impulse itself. The impact force of the impulsor was enough to provoke a material response while not saturating the microphone or causing damage to the sample. Validation of this table mounted IE test method was performed by Truesdale [29], using a similar setup. Using this system, three 6061 aluminum tubes and two 6061 aluminum bars were tested for accuracy

using the Timoshenko formulations for elastic moduli based on vibration response [38] and results compared with published values to with 4% error.

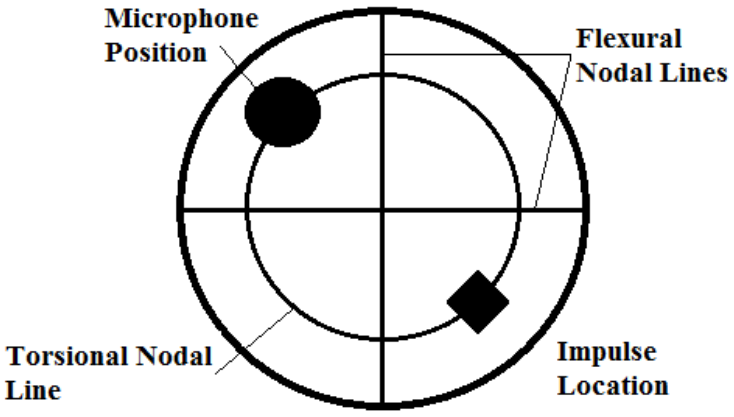

Figure 2.5: Sample graph showing locations of microphone and impulse point

Every impulse response was recorded by the microphone and checked for anomalies. Responses from poorly applied impulses that did not match the characteristic shape of a harmonic response were discarded. Impulses which did match were saved and a total set of 20 measurements were recorded for each sample measurement.

2.4 THE DROP WEIGHT IMPACT TEST

The test setup used for impacting the flat SiC_f/SiC_m TEP composite disks was a modified Instron Dynatup 8200-HE impact tower. The system consists of a striking piece (called a tup) that is fastened to a cart of adjustable weight which fits along two low-friction guide rails. The cart is hoisted to a specified height by a pulley system connected to a carriage. A simple push on the latch system that holds the cart and carriage together releases the cart. The cart would then fall towards the sample, which is clamped between a rigid

lower base and a rigid cover plate, the purpose of which was to keep the sample centered and fixed into position. Just before the impact tup strikes the sample, a pronged flag passes through an optical laser sensor that outputs binary wave data to the data acquisition (DAQ) unit. This provided the velocity of the cart just before impact. Upon impact, a load cell fastened at the base of the tup sent the DAQ load data throughout the entirety of the impact, which usually lasted on the order of 5~10ms. Two DAQ systems were used during these tests. The first DAQ system had a sample rate on the order of 10,000 samples per second and was used for the testing of Disk 1, Disk 2, and the first drop test of Disk 3. The second DAQ system used from Disk 3, Test 2 through the rest of the testing had a capture rate on the order of one million samples per second.

The standard used for the assembly of this test was ASTM D7136 [39] which covers drop weight impact tests of fiber reinforced polymer composites. The differences here are that ceramic composites are being investigated and that the impact tup used for this test is spherically capped as opposed to the hemispherical tup recommended in the standard. Also, the directive of the standard is the measurement of damage resistance, whereas the objective of this investigation is to apply and quantify a certain amount of load or damage and then monitor the change in IE results.

The sample holding fixture was designed such that the sample could be securely held in all directions and lightly supported around the circumference of the sample to prevent motion during and after impact. This differs from the ASTM standard in that clamps are not applied directly to the surface of the specimen. It was decided that the sample geometry and small size would not support this. Therefore, a cover plate was designed to fit around the sample, having pegs on the inside of the cover plate which fit

perfectly around the sample, keeping it in place. A polyethylene sheet was also used to soften the contact between the cover plate and the sample, ensuring equal pressure around the circumference. *Figure 2.7(A)* depicts this clamping configuration.

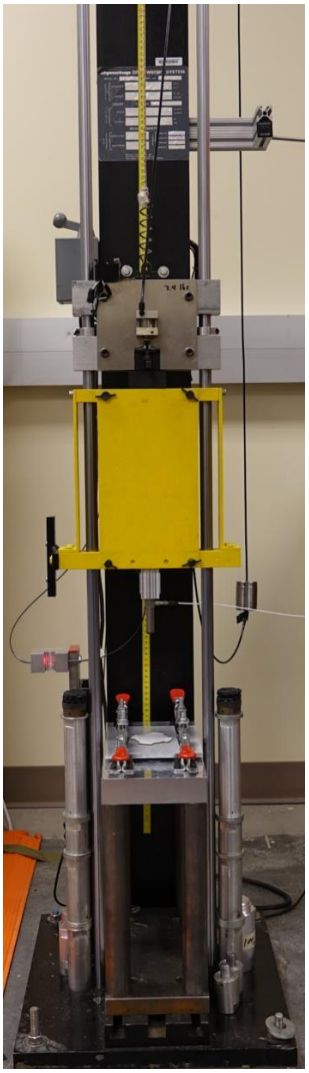

Figure 2.6: Instron Dynatup 8200HE

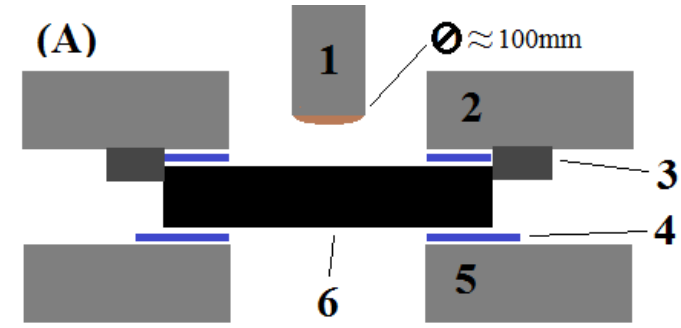

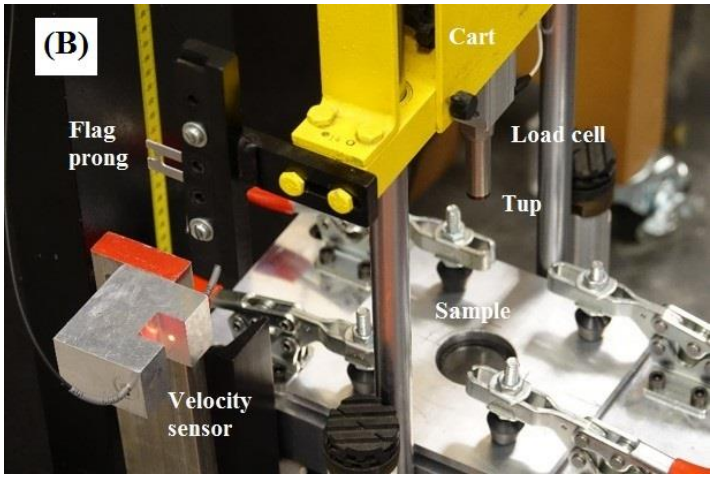

Figure 2.7: (A) Clamping system with 1: Impact tup, 2: Cover plate, 3: Centering pins, 4: Polyethylene gaskets, 5: Impact foundation, and 6: Test sample. (B) Instruments near impact zone

The impact tup used was a spherically capped tool steel tup from PCB with spherical radius of approximately 100mm. In this case, the tup was considered as a means

by which controlled damage could be applied to the specimen and a high surface area impactor seemed a logical choice to perform controlled experimentation on brittle ceramics such as SiC without destroying the sample. Therefore, a spherically capped tup was used that in terms of function falls between the hemispherical and flat tup geometries. In a paper that discusses this subject in the context of low velocity impacts, Cheon et al. [40] compare several impactor geometries and conclude that both the hemispherical and flat tup configurations "displayed similar energy dissipation and failure mechanisms." The difference found between the two was that the flat impactor induced comparatively less internal damage at the expense of more damage accumulation at the zone of impact. In this study no discernable damage was detected at the zone of impact.

The process of the drop tests proceeded as follows. First, the sample was loaded onto the sample holding fixture shown in *Figure 2.7(A)* and covered with the cover plate. The cover plate was then clamped down using the support clamps to lock the sample in place An overview of the instrumentation and fixtures near the clamping configuration is given in *Figure 2.7(B*). A plastic cover was placed over the cover plate temporarily to prevent the event of accidental drops hitting the sample. At that point the impactor was lowered to lightly touch the sample in order to gauge the zero position and adjust the flag prong to trip the velocity sensor within 6mm above the zero position as is standard. Next, the impactor system was slowly raised using an electric pulley system until the desired height was reached. This was measured by the measuring tape attached to the back of the device and a fixed position laser on the back of the carriage was used to indicate the distance. Knowing the position at which the tup contacts the sample, the total drop height could be easily found. Next, the velocity sensor and load cell were checked to ensure proper

working order before the DAQ was activated and the test was run by pulling the mechanical trigger bar which connects the cart to the carriage. After the test, the cart was carefully pulled back up and locked into the carriage and the sample was removed for inspection and IE.

2.5 TEST SEQUENCE, ANALYSIS AND RESULTS

Two disks (1 and 2) were put under the same loading circumstances: two tests at drop heights of 2cm and 4cm respectively under similar loading conditions. Disk 3 was impacted repeatedly at a drop height of 2cm five times. IE measurements were taken prior to each impact and once after the last test, as well as images of the sample. During IE, each sample was centered on the suspension lines by measurement with the impact side facing up and oriented in the same direction. While the determination of the nodal lines of an isotropic flat disk are arbitrary, it was considered best to align these composite disks along the crossed suspension wires in line with the visible portions of the woven fibers near the surface of the sample. Also, each sample was tested in sequence and with similar loading orientations.

The back face of the composite specimens is the best visible indicator of damage on the sample. Four radial cracks appeared on the surface of the back face after a sufficient amount of damage was applied to the disk. Testing continued after the appearance of the radial cracks due to the fact that the structural integrity of the sample was maintained. Only after complete fragmentation of the disk did testing end. *Figures 2.8-2.10* showcase the visible crack progression for each sample following impact testing.

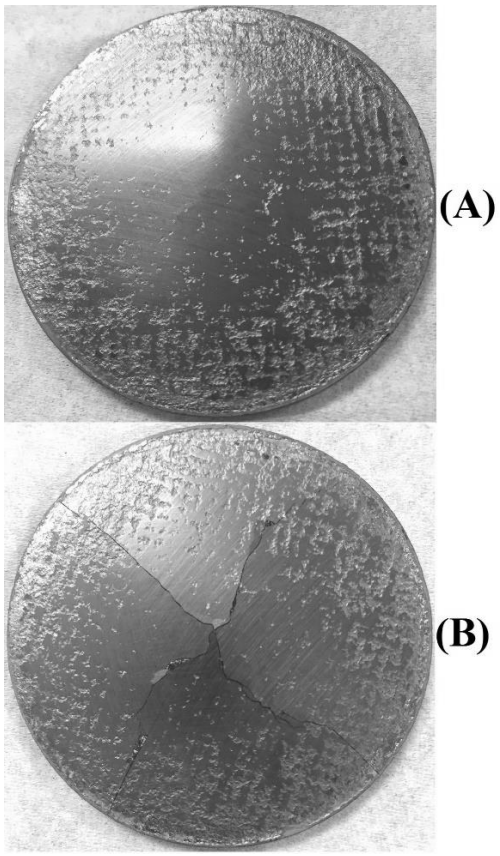

Figure 2.8: Disk 1 Back face. (A): After 2CM Impact, (B): After 4CM Impact

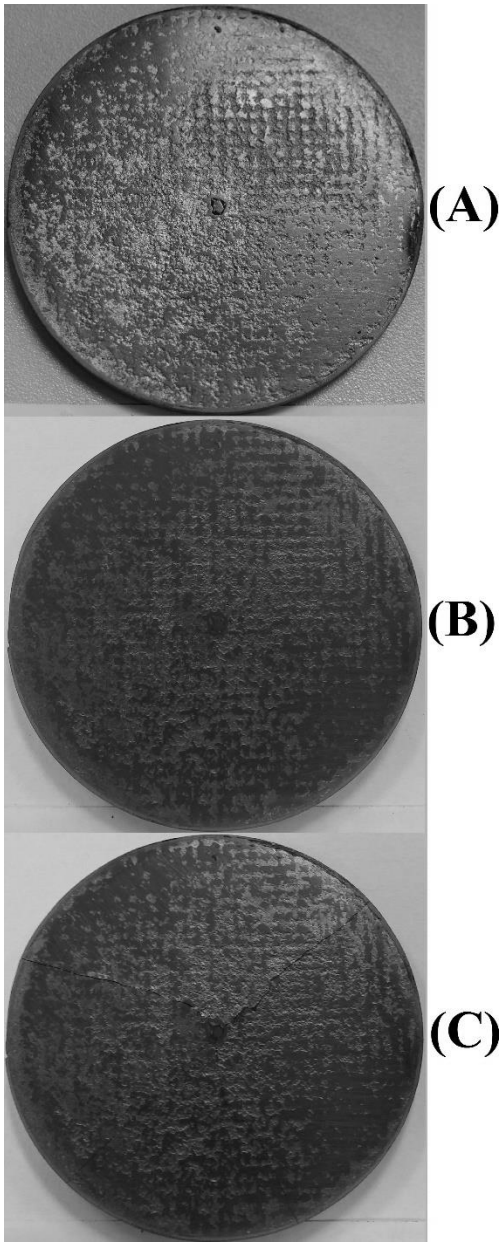

Figure 2.9: Disk 2 Back face. (A): Pristine, (B): After 2CM Impact, (C): After 4CM Impact

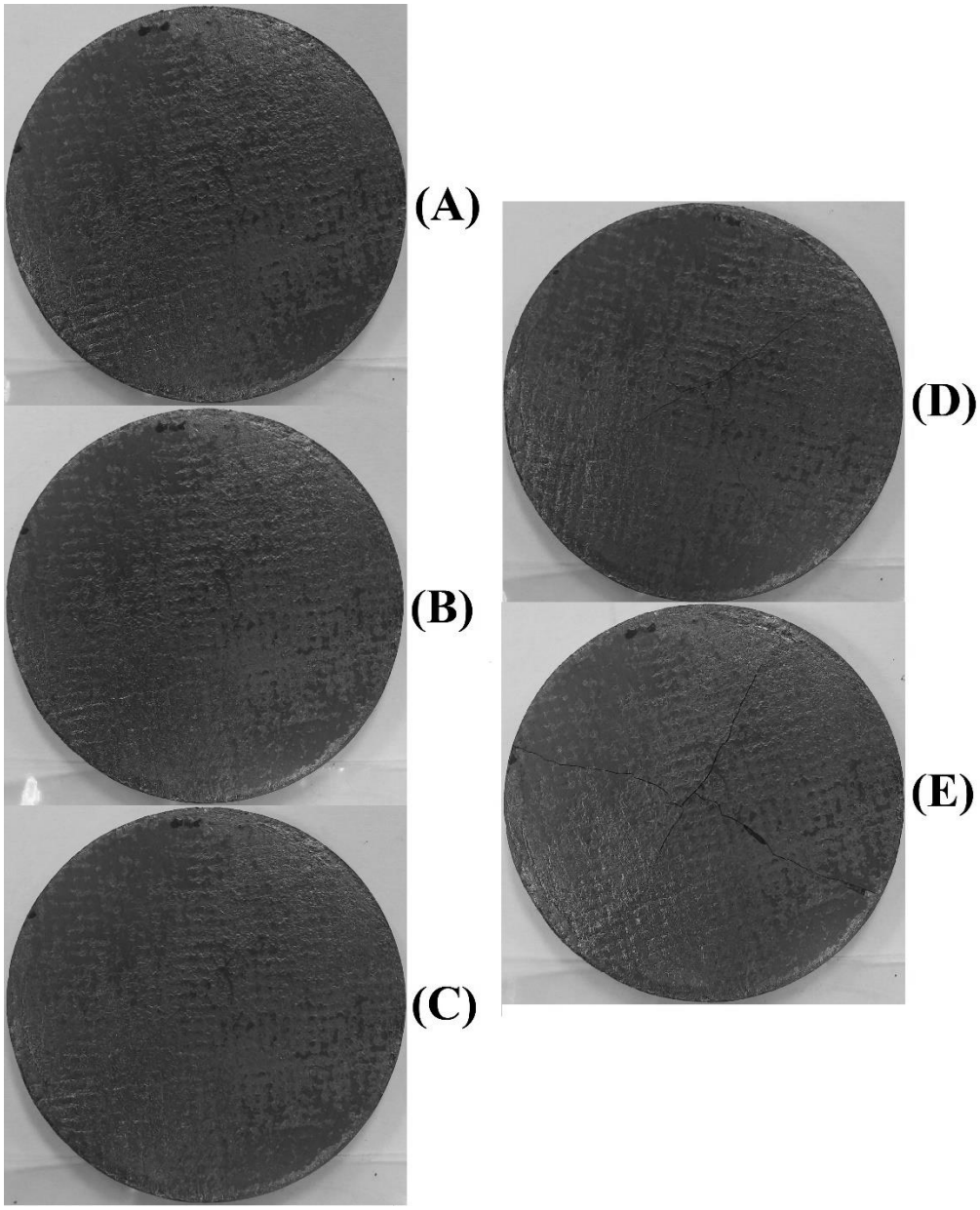

Figure 2.10: Disk 3 Back face. (A)-(E) follow tests (1)-(5).

Data analysis on the load and velocity data was performed in order to reveal the load, velocity and displacement information and calculate estimated absorbed energy in accordance with ASTM D7136. First, load data was converted from a voltage to force in Newtons according to the manufacturer specifications of the load cell. This was divided by the mass of the cart, which was constant throughout all tests at 2.76kg, and then integrated numerically to find change in velocity according to Newton's second law of motion. The

velocity sensor data was then used to supply the calculation with an initial velocity. Knowing the distance between the two prongs of the flag, a simple calculation was employed using the timestamps of the velocity sensor data to find the velocity of the cart just before impact. A modifier including the acceleration of gravity and the known time before impact was added to this number to estimate initial velocity at impact, and *Equation 2* was used for this calculation. Next, the measured impact energy of the event was calculated. Using the impact location as the reference position δ_i, *Equation 3* was used to calculate the displacement versus time, and these values were finally used in conjunction with the velocity analysis according to *Equation 4* to find the absorbed energy versus time. Total absorbed energy was collected by subtracting the absorbed energy at the end of the test from the value at the beginning of the test (usually zero) [41]. Graphs showing load and energy versus time data for each specimen are provided in Figures 11-14. A chart showing drop height, maximum load and absorbed energy is also provided with IE data in *Table 2.1*.

$$v(t) = v_i + gt - \int_0^t \frac{F(t)}{m} dt \qquad (Eqn\ 2)$$

$$\delta(t) = \delta_i + v_i t + \frac{gt^2}{2} - \int_0^t \left(\int_0^t \frac{F(t)}{m} dt \right) dt \qquad (Eqn\ 3)$$

$$E_a(t) = \frac{m(v_i^2 - v(t)^2)}{2} + mg\delta(t) \qquad (Eqn\ 4)$$

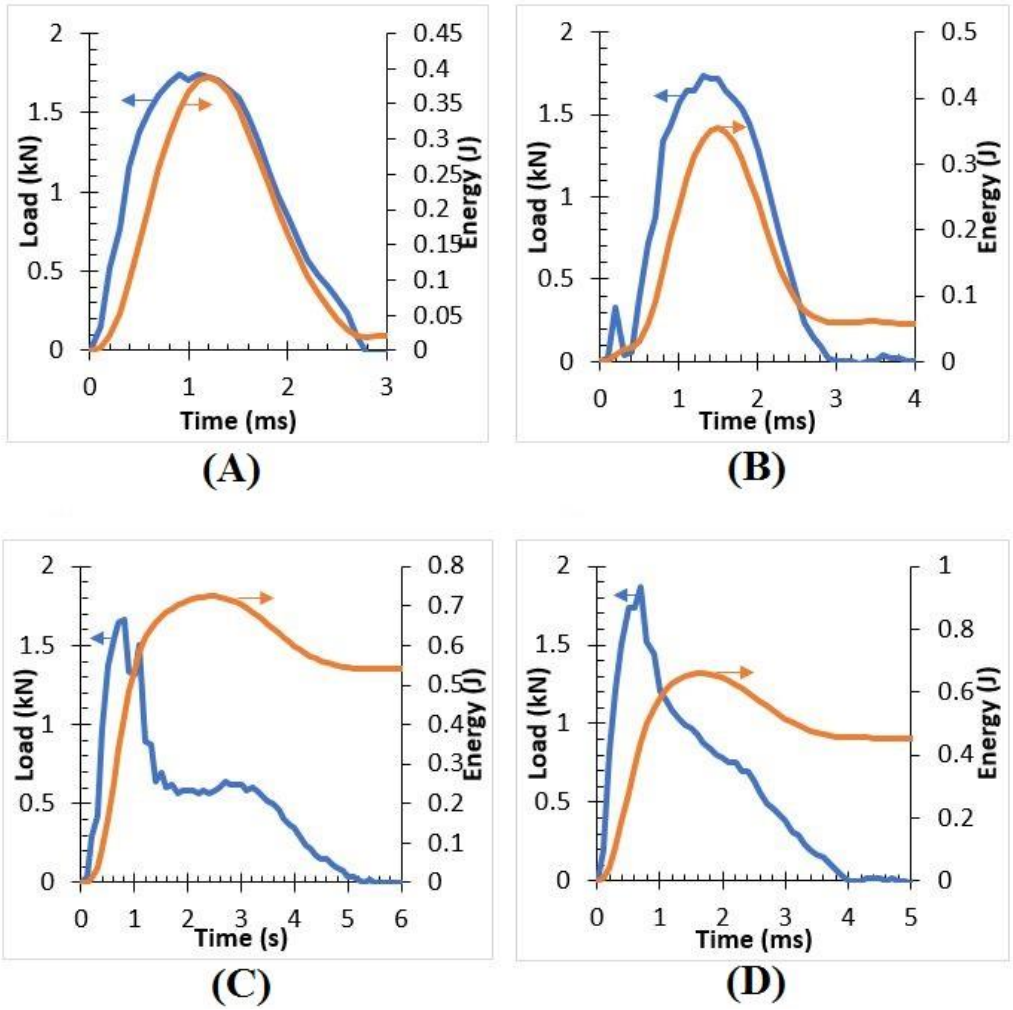

Figure 2.11: (A) Disk 1 Test 1 Load/Time, (B) Disk 2 Test 1 Load/Time, (C) Disk 1 Test 2 Load/Time, (D) Figure 2.14: Disk 2 Test 2 Load/Time

From *Figure 2.11*, it is shown that higher drop heights provide more brittle impact regimes. This can be seen by the differences between the 2cm drop tests and the 4cm drop tests. After each 2cm impact, the load diagrams yield nearly symmetric bell-shaped curves, which represent high energy deflection and low energy absorption [42]. Compare this with the energy curves and energy absorbed of those tests. Tests 2 for both disks show a much different outcome following the 4cm drops. These load curves are very asymmetrical and are accompanied by higher energy absorption.

Figures 2.12 and *2.13* provide an overview of the load and energy results of Disk 3. A few anomalies in this test sequence are important to point out: First, Tests 2 and on were conducted with a DAQ which had a higher sample rate on the order of one million samples per second compared to the previous DAQ which captured samples at a rate on the order of 10,000 samples per second. Also, during Test 2 a collection error occurred which prevented the recording of the last portion of the load curve. Because of this, the energy curve is similarly affected. It is likely that the load curve for Test 2 should terminate somewhere between Tests 1 and 3, and that the energy curve should behave similarly.

It is convenient in *Figure 2.12* to watch how the load curves change with progressive testing. As the disk is impacted, the load curves reach lower maximum loads, while stretching out the impact over a longer period of time and becoming more asymmetric. This may indicative of the sample moving from a matrix dominated cracking regime to a fiber dominated deformation regime as the damage progression moved from a phase of breakage initiation to breakage spreading [43]. The fracture toughness itself is highly dependent on the interphase, the quality of which is a difficulty of the TEP process. As the sample absorbs energy, it becomes less brittle and more tough which makes the disk more effective at absorbing energy. A review of *Figure 2.13* verifies this analysis. As the sample is progressively damaged, the energy absorbed appears to move from a consistent 0.065J to higher values. The curves also appear to begin stretching out to longer periods after Test 3.

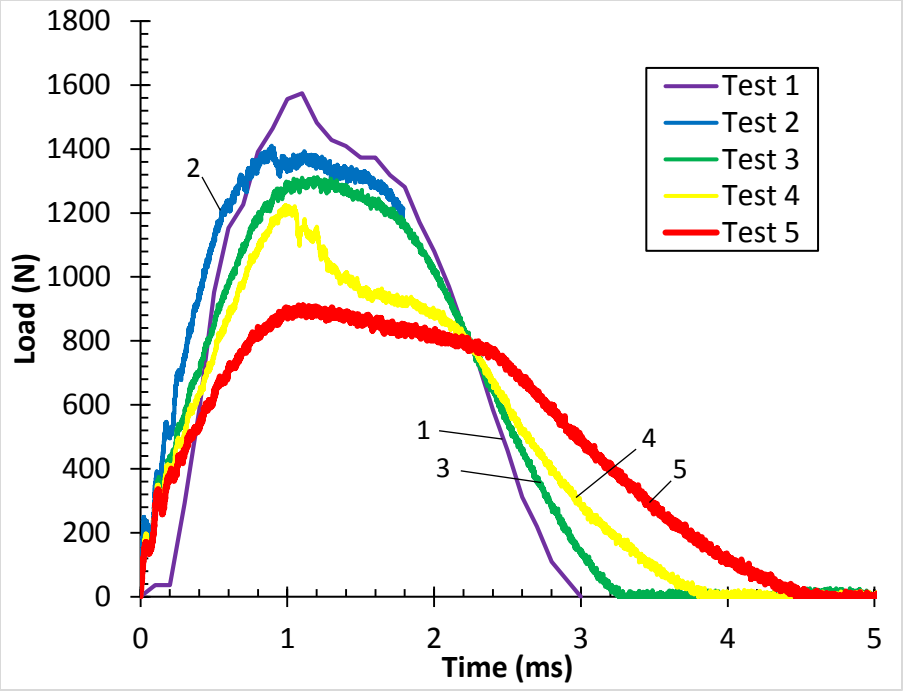

Figure 2.12: Load/Time Graph including all load data from Disk 3 testing. Test 2 terminates early due to DAQ issue.

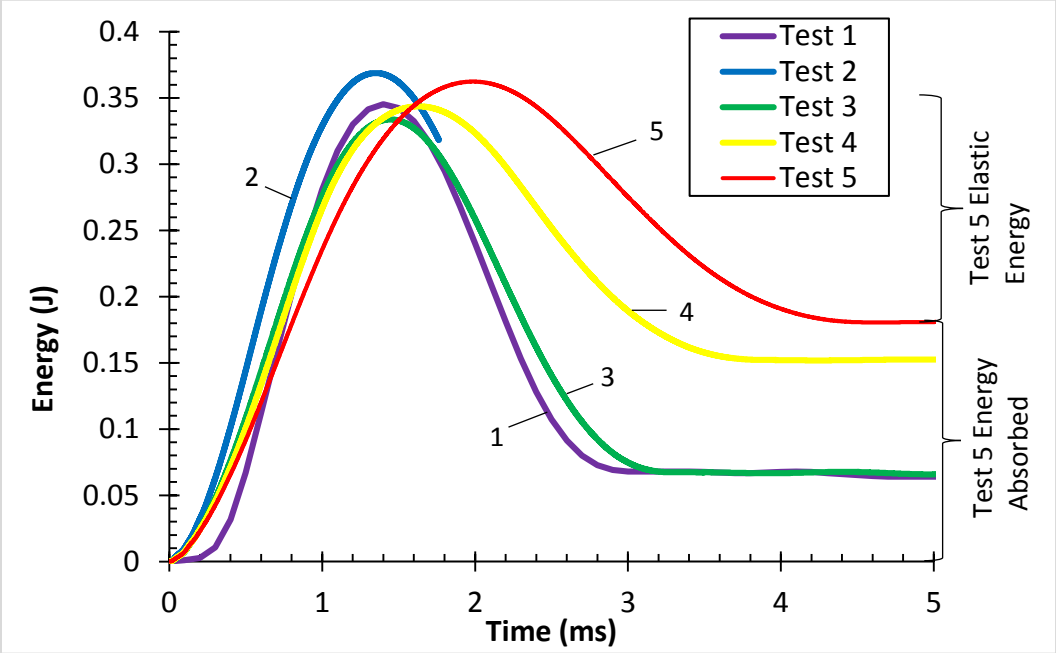

Figure 2.13: Energy/Time Graph including all energy data from Disk 3 testing. Test 2 terminates early due to DAQ issue.

IE data was collected following each test and is provided in the scatterplots in *Figures 2.14, 2.15* and *2.16*. The IE measurements were very repeatable and errors in measurement in every case were on the order of 2-3 Hz or within 0.03% of the lowest recorded values. Therefore, measurement error is omitted here as negligible. *Figure 2.14* shows IE frequencies and associated dampings for testing of Disks 1 and 2. It is clear that the frequencies for both samples decrease at an almost identical pace. Also, change between IE measurements become much different after the 4cm drops, in which the samples absorbed more energy as previously discussed. This is also seen in *Figure 2.14* (C) and *(D)*wherein damping rises at a much larger pace than in the 2cm drops.

IE results from the testing of Disk 3 are shown in *Figures 2.15* and *2.16*. Frequency and damping results show consistent and progressive changes throughout the course of testing. As damage is produced in the sample, frequency falls and damping rises. This agrees with the IE data from Disks 1 and 2. In fact, frequencies for all three samples begin in a similar vicinity and then appear to fall in similar proportion to damage absorbed. The same could be said for damping. *Figure 2.17* shows a plot of change in frequency over total energy absorbed by each sample. The energy absorbed value for Disk 3, test 2 had to be estimated based on results from tests 1 and 3. Because there are clear trends shown between damage absorbed and IE results, it was decided that test 2 must have energy absorption results similar to tests 1 and 3, and *Table 2.1* and *Figure 2.17* reflects this assumption while indicating that this is an assumed value.

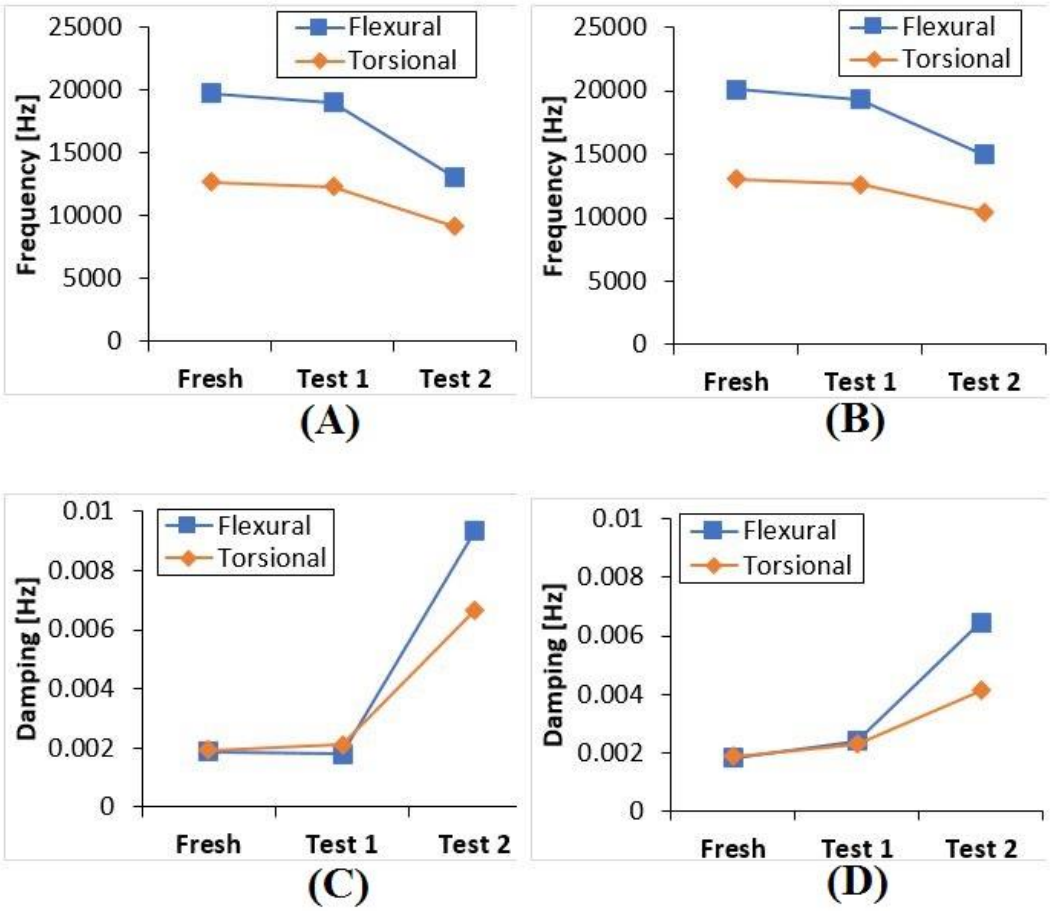

Figure 2.14: (A) Disk 1 IE Frequency, (B) Disk 2 IE Frequency, (C) Disk 1 IE Damping, (D) Disk 2 IE Damping

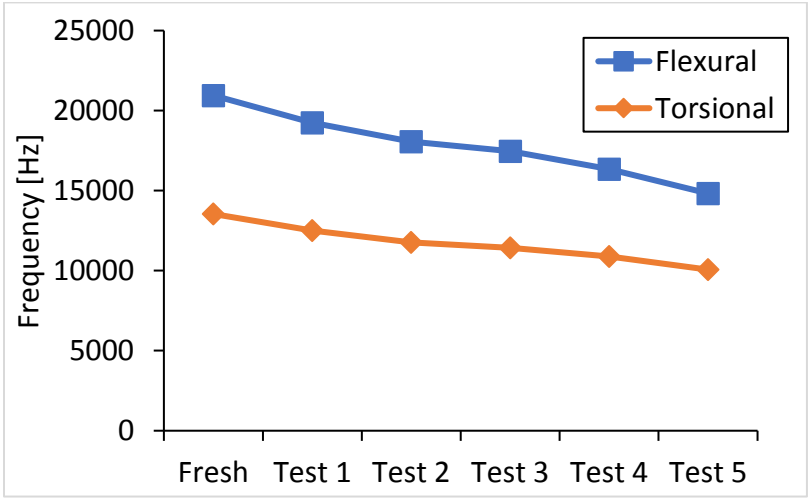

Figure 2.15: Disk 3 IE Frequency as recovered following the end of each test.

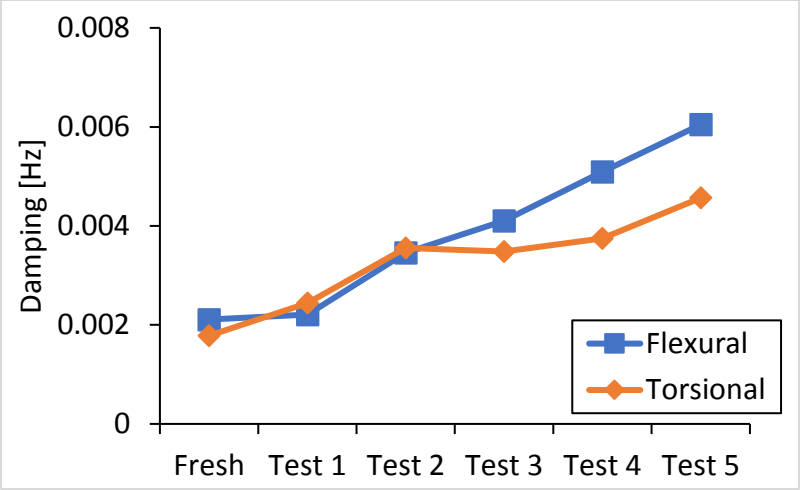

Figure 2.16: Disk 3 Damping as recovered following the end of each test.

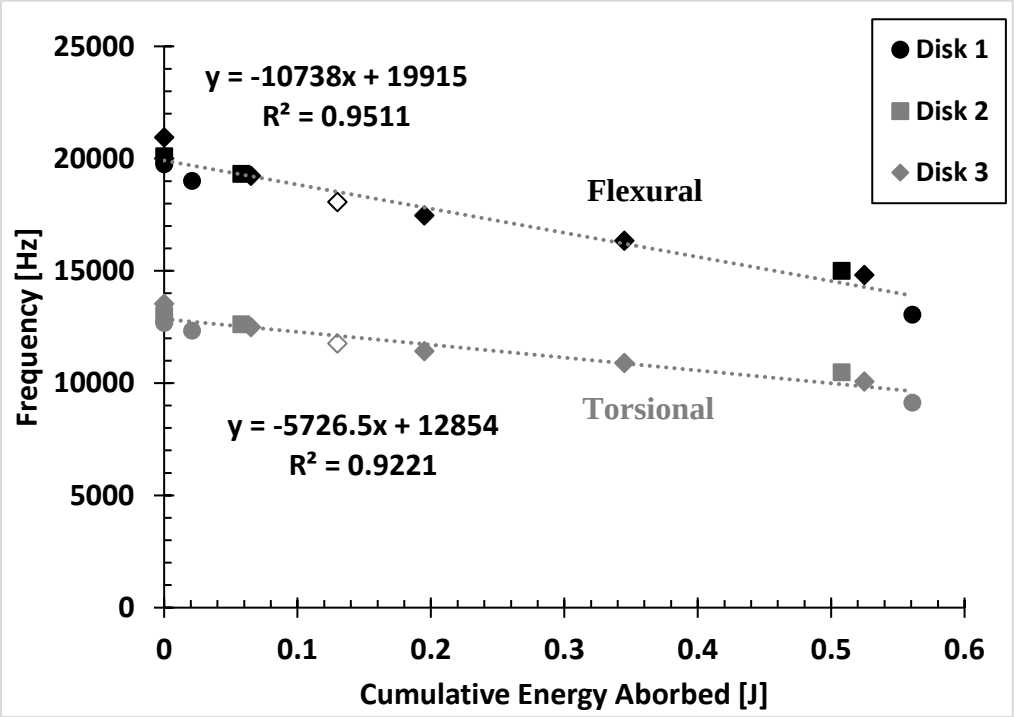

*Figure 2.17: Flexural and Torsional frequency change over cumulative absorbed energy. Torsional frequencies shaded with lighter color to distinguish from flexural. *Disk 3, Test 2 value is hollowed to indicate assumed energy absorption.*

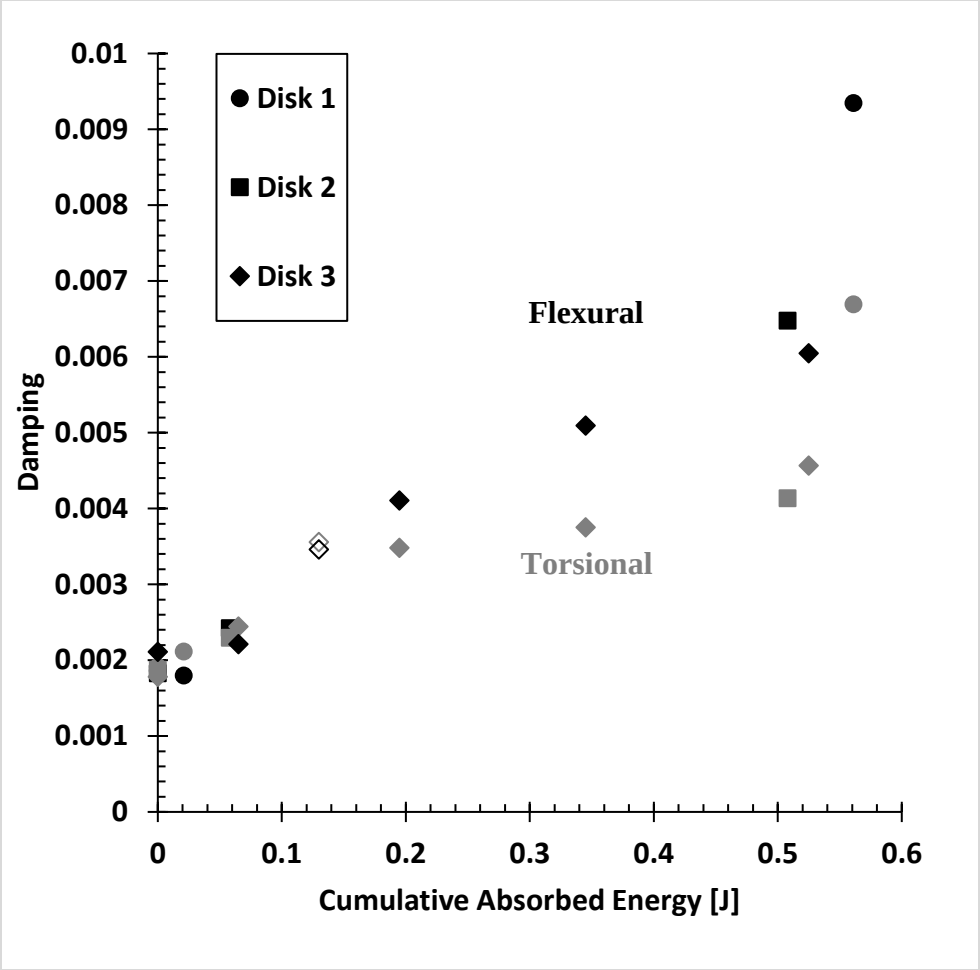

*Figure 18: Flexural and Torsional damping change over cumulative absorbed energy. Torsional dampings shaded with lighter color to distinguish from flexural. *Disk 3, Test 2 value is hollowed to indicate assumed energy absorption.*

Figure 2.17 shows a linear trend between the frequency change experienced by the composite disks and the cumulative energy absorbed. This trend was calculated using Microsoft Excel via the least-squares method and appears to be very stable to within a coefficient of determination of 0.95 for flexural and 0.92 for torsional frequencies. This shows that the energy absorbed by SiC_f/SiC_m composite disks are directly related to the change in frequency observed by IE. *Figure 2.18* shows a less predictable trend between the damping and energy absorbed.

*Table 2.1: Summary of Impact and IE Data. *Estimated Value*

Sample/Test Number	Drop Height [cm]	Maximum Load [kN]	Energy Absorbed [J]	Flexural Frequency [kHz]	Torsional Frequency [kHz]
Disk 1 / Pristine	N/A	N/A	N/A	19.7	12.7
Disk 1 / Test 1	2	1.74	0.018	19.0	12.3
Disk 1 / Test 2	4	1.67	0.541	13.1	9.1
Disk 2 / Pristine	N/A	N/A	N/A	20.1	13.0
Disk 2 / Test 1	2	1.74	0.058	19.3	12.6
Disk 2 / Test 2	4	1.87	0.453	15.0	10.5
Disk 3 / Pristine	N/A	N/A	N/A	20.9	13.5
Disk 3 / Test 1	2	1.57	0.066	19.2	12.5
Disk 3 / Test 2	2	1.41	0.066*	18.0	11.8
Disk 3 / Test 3	2	1.31	0.066	17.5	11.4
Disk 3 / Test 4	2	1.22	0.152	16.3	10.9
Disk 3 / Test 5	2	0.91	0.181	14.8	10.0

2.6 CONCLUSIONS

It is clear that as the disks absorb more energy, frequency and damping of the IE results show predictable change. As damage occurs in the SiC_f/SiC_m composite, cracking within the volume of the material lead to a change in structural integrity which can be tracked using impulse excitation. It is shown that after each impact, flexural and torsional frequencies fall and damping rises in each case, and that this change is directly proportional to energy absorbed. Furthermore, it is apparent that the energy absorbed by these

composites can be quantified via frequency change. This research suggests the possibility that a specimen in a state of unknown induced damage can be measured in this manner and that the damage, quantified in terms of frequency change and energy absorbed, can be estimated and evaluated. However, damping does not show a stable trend with energy absorption. There does appear to be a relationship in that damping in the sample rises with accumulation of damage, but it does not fit as well in a direct relationship. It is likely that other factors, such as type, distribution and location of damage affects the damping signal. If this is the case, then it may mean that recorded damping represents a more promising method by which damage can be evaluated in detail. Future research may uncover critical correlations between damping behavior and specific types and severity of damage.

It is probable that material properties and the geometry of the composite control the change in frequencies and damping, and that a holistic evaluation of a SiC_f/SiC_m composites may yield methods by which pieces can be tested for manufacturing defects and prior damage before use in application. For example, it is shown here that the flexural frequencies of these composites were measured in a similar range on the order of 20kHz. If a similar sample is measured and found to have a flexural frequency much lower than this value, then it is justified to conclude that there is some difference in the material, and the correlating estimation of energy absorbed may be useful in determining whether the material is still fit for service. The challenge with such an analysis is that a great deal of testing would be required to properly differentiate between allowable and non-allowable frequencies. It may also be possible to use IE analysis to predict failure behavior under specified loading conditions, or to analyze the crack healing behavior of some related SiC materials [44].

The fact that change in frequency can be used to estimate energy absorbed as damage by a specimen has large implications in the field of damage monitoring. Not only can frequency analysis of SiC_f/SiC_m composites suggest that damage has occurred, it can also suggest the severity of damage. If future research can reproduce these results in other sample geometries and qualify failure criteria under specific loading conditions in terms of total absorbed energy, then it becomes possible that IE can be used to estimate crucial aspects of material performance. The severity of accidental damage, structural stability and time to failure are examples of what could be possible to estimate using this method.

CHAPTER 3

SIZE EFFECT AND FAILURE ANALYSIS OF SiC_F/SiC_M TUBES UNDER INTERNAL PRESSURE LOADING

3.1 INTRODUCTION

As previously discussed, SiC_f/SiC_m composites are being researched as candidates for nuclear fuel cladding in the creation of ATF. Therefore, it is necessary to qualify these composites using the proper geometry and conditions necessary to meet that goal. One important stress state that fuel cladding must endure during accidents is internal pressure loading. In accident situation, pressures on the inside of the cladding can exceed the outside pressure and cause the cladding to burst. Work has been focused on researching the elastic moduli, leak rate and burst pressures of SiC_f/SiC_m claddings under load [45,46,47].

In the event of any accident within a nuclear reactor, the cladding must be able to contain the fuel and prevent it from contaminating its surroundings [48]. SiC_f/SiC_m is a good candidate for this role due to several reasons. First, upon passing the proportional limit strain (PLS), the composite begins to break down gracefully as the woven fibers begin to take load. This exchange allows the composite structure to last much longer under increasing load than a monolithic structure. Also, when ruptures in fiber tows begin to occur and propagate, the composite is capable of arresting the spread of failure and can keep it localized to one region [49].

In this study, the size effect of SiC_f/SiC_m tube geometries were investigated by repeatedly measuring burst ultimate tensile stress (UTS) from internal pressure loading as an indicator of strength. These were loaded using a hydraulic internal pressurization method in order to determine ultimate strengths under hoop loading. Once burst, the destroyed portion of the tubes were cut off producing one or more additional samples. Burst testing continued in this manner until the remaining pieces were too short to test.

3.2 THE SIC_F/SIC_M TUBES

Three samples listed here as Tubes 1, 2 and 3 were provided by General Atomics. The SiC_f/SiC_m composite tubing used was manufactured via CVI and were composed of woven layers of stoichiometric grade Hi-Nicolan Type S fibers woven in a tubular geometry using a mandrel to define the inner and outer diameters of the fiber preform. This was followed by chemical vapor deposition of pyrolytic carbon to a thickness of less than 500nm. Finally, the CVI process was used to deposit a stoichiometric β-SiC matrix using decomposition of methyltrichlorosilane. Each of the three samples tested were manufactured within the same batch under one gas flow, pressure and temperature regime which was expected to make each sample uniform with respect to material quality [50]. However, it is important to note that these specimens are non-standard, early generation material from General Atomics and are not representative of current fuel cladding engineered design. In particular, fiber architecture and defect distribution appears to have led to a material showing roughly 2x reduced UTS and an expectedly greater defect distribution [51].

Each tube originally measured approximately 28cm in length, with an outer diameter of 11mm and wall thickness of 1.5mm as measured by calipers. Measurements of the samples were taken with a special micrometer designed for measuring inner diameters and with calipers to get the dimension of the outer diameter. These measurements were taken using an average of multiple measurements collected across the length and around the circumference of the specimens. In this case, the inner and outer diameters of the SiC tubes in question are fixed due to geometric constraints for the cladding, but the length of these claddings can be adjusted in the lab for testing. In reality, the length of the cladding is also fixed by the length required by the reactor, but to test claddings at that scale (on the order of 4 meters) would require extensive manufacturing and expenditure. Instead, shorter samples can be tested in order to predict the overall strength of a material in the absence of defects, and to view the change in strength as defects are removed from the specimen.

3.3 DAMAGE BEHAVIOR AND THEORY OF SIZE EFFECT

When pressurized, a SiC_f/SiC_m composite tube follows a predictable pattern of damage and failure. In his work on the subject, Alva [52] details this pattern of behavior by reviewing the AE data collected from internal pressure tests and concludes that there are three primary regions of damage accumulation leading to failure of the specimen. First, as the sample begins to be loaded the matrix material takes the brunt of the pressure in the elastic region, providing little acoustic emission events and exhibiting a linear stress/strain relationship. Once the load reaches the PLS, the matrix begins to break up and shifts load to the fibers. This is known as the matrix-driven region because of the prevalence of matrix cracking which yields a large amount of AE events. Finally, once the matrix has completely broken up and shifted load to the fibers, a region of behavior known as the quasilinear or

fiber-driven region begins. Finally, the sample is burst at its ultimate tensile stress (UTS). *Figure 3.1* displays a stress/strain and cumulative AE energy curve that depicts the boundaries of these three regions.

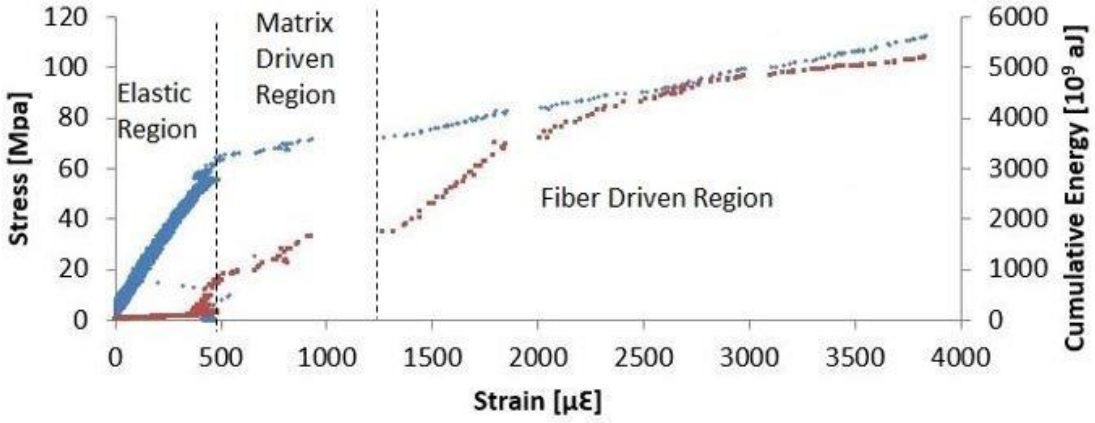

Figure 3.1: Tube 3a Stress/Strain curve with AE as example of internally loaded SiC_f/SiC_m composite. Dashed indicators added to show the three regions of failure behavior.

The mechanics used to analyze these composite tubes were taken from the field of thick-walled pressure vessels, due to the thickness ratio of these samples. As such, Lame's equation was used to calculate hoop stress inside the tubes and is shown in *Equation 5*. This is a general equation to calculate hoop or tangential stress within an open-ended tube with an applied external and/or internal pressure, though it assumes that the material is an isotropic, homogeneous material. Assuming no applied external pressure and the outer radius as the radius being measured, *Equation 5* simplifies to *Equation 6*, where P_i is internal pressure, r_i is inner radius, and r_o is outer radius.

$$\sigma_\theta = \frac{P_o {r_o}^2 - P_i {r_i}^2}{{r_o}^2 - {r_i}^2} + \frac{(P_o - P_i){r_i}^2 {r_o}^2}{{r_o}^2 - {r_i}^2}\frac{1}{r^2} \quad (Eqn\ 5)$$

$$\sigma_\theta = \frac{-2P_i {r_i}^2}{{r_o}^2 - {r_i}^2} \quad (Eqn\ 6)$$

In the context of this study, a discussion of the Kaiser effect is in order. Originally developed in in the context of rocks and mining [53], the Kaiser effect describes a behavior of ceramic materials in which specimens that are loaded multiple times do not produce additional AE events unless the maximum threshold of the last loading program is surpassed. The Kaiser effect has been related to the behavior of composite materials [54,55] and has been observed in SiC_f/SiC_m composite materials [56]. As such, iterative testing on cuts made from an original composite specimen may not be compared to the original during pre-PLS or matrix-driven regime and can only be best compared in terms of UTS. However, the presence of the Kaiser effect up until the previous UTS of the last sample would verify that the sample has been uniformly loaded.

Size effects are material dependent qualities that change based on the size of the material in question. The size effect is due to the prevalence of defects within the material [57]. The longer a specimen is, the more likely a serious defect will be present somewhere along the length, presenting a statistical likelihood of lower ultimate strength in larger samples. Unnthorsson et al. [23] describe the three stages of life of composite structures as production of structural fibers, assembly of the full composite structure, and service life after manufacturing. What is exceptional about this life cycle compared with most isotropic materials is that service life represents the last stage of life, meaning that defects have ample opportunity to form within the structure. Unnthorsson et. al. continue with an

analysis of the manufacturing of composite materials, in which they catalogue a host of defect types and how they can form.

These defects become a concern during the service life of the material, where in the absence of NDE damage detection they can go unnoticed. When placed under uniform internal pressure loading the stress will overcome the material in the defective area at that a much lower stress than the rest of the material, leading to a failure of the cladding on a macro-scale. As SiC_f/SiC_m composite manufacturing matures it is likely that these defects will decrease both in prevalence and severity.

In a homogeneous and uniform material, failure will occur at the point of greatest weakness, which in the case of monolithic ceramics is typically a defect or position of pre-existing damage. Because the probability of defects and defect concentrations increases with sample size, a noticeable drop in ultimate strength is associated with larger ceramic materials compared to smaller ones. However, CMC composites such as SiC_f/SiC_m are expected to show less correlation between sample size and UTS because of the heterogeneity of the structure of the material. In their analysis of the macroscopic size effect of SiC composites, Calard & Lamon [58] state that the composite geometry reduces the impact of defects because the breakdown of the matrix prior to UTS eliminates the contribution of flaws in the matrix and that individual fiber breaks leading up to UTS removes the contribution of an undetermined number of flaws in the fibers. Because of this, they note that the ultimate tensile stress relies on the strength of the fibers, and that UTS is usually dependent on the lowest extreme of the fiber strength within a material. However, because Nicolan SiC fibers are high quality and very similar to one another, the strength scatter between them should be limited. Calard & Lamon back up this assertion

with tensile strength data collected from sequential testing of 2D woven SiC_f/SiC_m bars loaded parallel to tow direction that show little variation of UTS between sample lengths. Another study performed by Nozawa et. al. [59] performed an experimental analysis of tensile strength based on varying gauge length between several geometries of woven SiC_f/SiC_m bars ranging from 15mm to 45mm, but results similarly do not show an apparent length dependence in this range.

3.4 TEST PROCEDURE

Before the composite tubes can be tested, they must first be catalogued and prepared. First, measurements and images were taken, followed by a light cleaning and the attachment of a strain gauge(s) to the surface. The strain gauges would eventually be connected to a Wheatstone bridge and data from them would be recorded by a DAQ system. Next, a speckle pattern for use with DIC was applied to the surface of the sample before it was attached to the rig in an orientation that would not allow the strain gauge to obscure DIC results. At this point, AE sensors were attached directly to the sample surface and tested using a pencil lead break test.

The burst rig used in this study was similar to the hydraulic internal pressurization method developed by Shapovalov [60]. The composite tube was fixed with zero axial stress between two rigid supports with a flexible PVC tubing (bladder) positioned on the inside of the tube. The tube was first filled with oil at no pressure to remove the presence of air and then additional oil was pumped in into the bladder, forcing it to expand and fill the inside of the tube. The bladder material is thin and can be assumed to be incompressible,

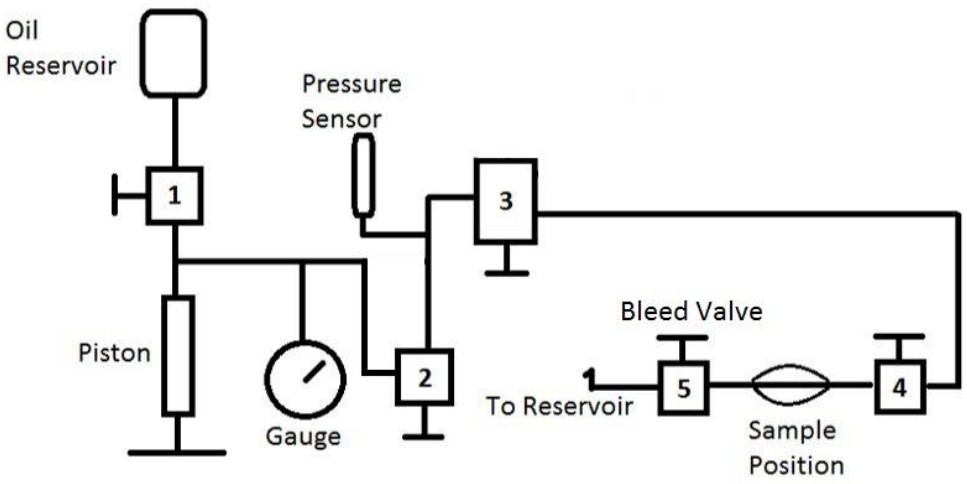

Figure 3.2: Burst rig oil flow diagram

allowing a pressure reading taken from a pressure sensor attached to the system to provide the data used to calculate the stress on the sample. The sample is loaded in this manner until failure. Shapovalov validated this test method by placing an aluminum tube on the fixture and running tests in order to compare measured results with published values. Young's modulus and Poisson's ratio for the aluminum sample were recorded within 4% of the published values, and uniformity of the pressure distribution was confirmed by multiple hoop direction strain gauges across the length of the sample which showed agreement to within 3% at high pressure. This confirms the validity of this test method in the context of this study, which reviews the behavior of composite tubes as long as 28cm. As previously mentioned, the pressure, strain gauge, DIC, and acoustic emission data were recorded from each test.

After a tube was loaded to failure in this manner, it would be removed from the test rig and used for further testing. After pictures were taken, the sample would be reviewed to see enough unbroken material remained for further testing. If a length of at least 3cm of the material passed inspection, the sample would be carefully sectioned using a diamond

saw. A 1cm distance between the edge of the cut and the nearest point of failure was always kept in order to prevent excessive failure of fiber tows from being present in the cut sample.

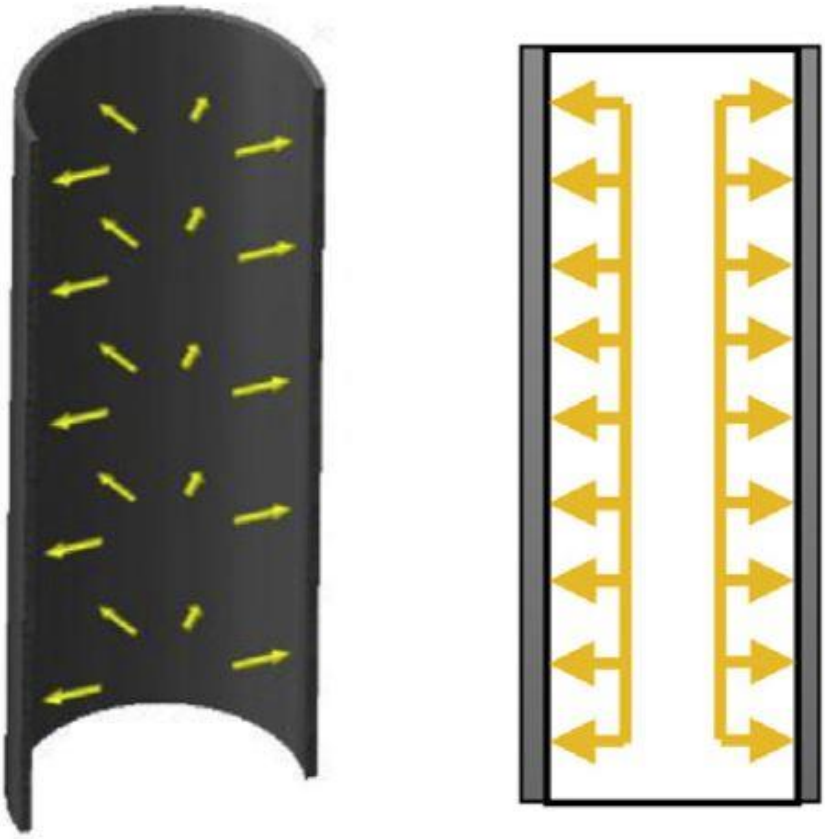

Figure 3.3: Internal pressure boundary experienced by the samples [15]

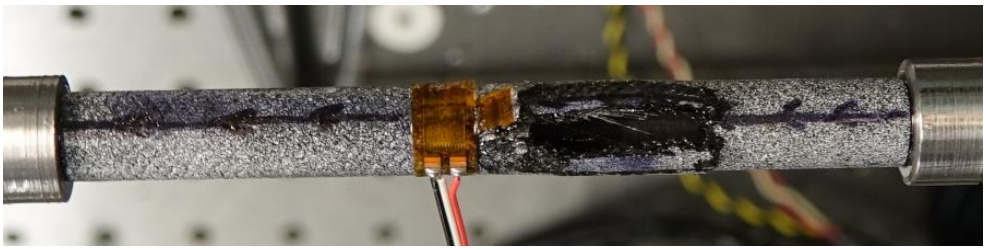

Figure 3.4: Tube 2c attached to fixture following failure

3.5 EXPERIMENTAL RESULTS AND ANALYSIS

Tubes 1, 2 and 3 were each loaded to burst sequentially until no unbroken portions of adequate length were left on the sample. Each sequential burst is labelled with an alphabetic tag in the order in which the burst tests were conducted. Images of the failed samples along with a graphical indication of the progression of failure in each specimen are provided in *Figures 3.6, 3.9* and *3.10*. The tubes exhibited several kinds of failure modes, namely axial hinging, edge breaks, and axial splits. Examples of each type of failure are presented in *Figure 3.5*, with a summary of burst data and failure type presented in *Table 3.1*.

Figure 3.5 displays modes of failure of the composite tubes observed in this investigation. When the material approaches the failure point, a point of weakness within the material begins to propagate damage. This may be initiated by a fiber tow breakage within the fiber-driven region or by continuity of cracks carried over from the matrix-driven region. At this point, fiber tows begin to break in series starting from the initiation point and progress axially along the length of the tube in both directions. Each sample exhibited the ability to arrest the progression of these cracks by diverting the failure propagation into the hoop direction, as is seen in failure 1, 2, 4, and 5. This is desirable in damage tolerant composites because the failure is not allowed to propagate across the entire structure [61].

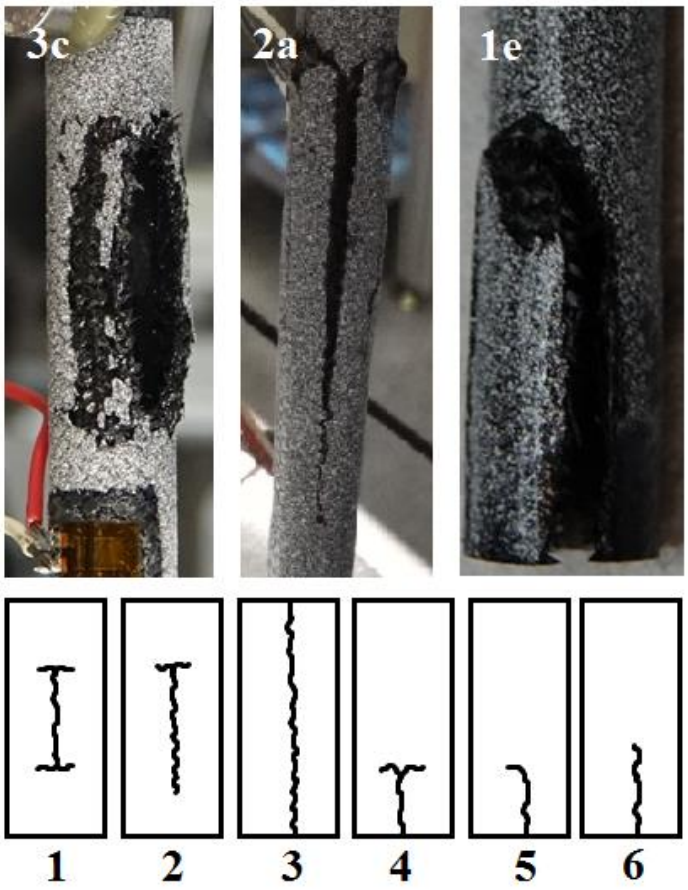

Figure 3.5: Various types of SiC_f/SiC_m tube failure with some examples. 1: Fully-arrested, 2: Semi-arrested, 3: Unimpeded, 4: Arrested edge, 5: Curved edge, 6: Unimpeded edge.

If not arrested, these cracks can continue along the entire length of the sample leading to a complete split of the specimen, or end early if enough stress has been relieved, as exhibited in the failure types 2 and 6. The failure of Tube 2a is also shown in *Figure 3.5* and provides an example of a situation in which the sample successfully arrested the crack in one direction but failed to arrest it in the other direction, allowing the split break to continue. Edge breaks, like that seen in the failure of Tube 1e, likely begin at or near the very edge of the tube. This could be due to the presence of defects caused by the sectioning process or due to a pre-existing defect located close to the edge of the sample. If the defect

is caused by the sectioning process, this could lead to failures of shorter specimens at a lower stress states than previous breaks. A likely example of this can be seen in *Figure 3.11*, which displays the outer diameter UTS of each sample by tube length. Tube 1e is shown there as failing at a fairly lower stress level than other samples close to its length, and contrary to the trend displayed by the rest of the tests.

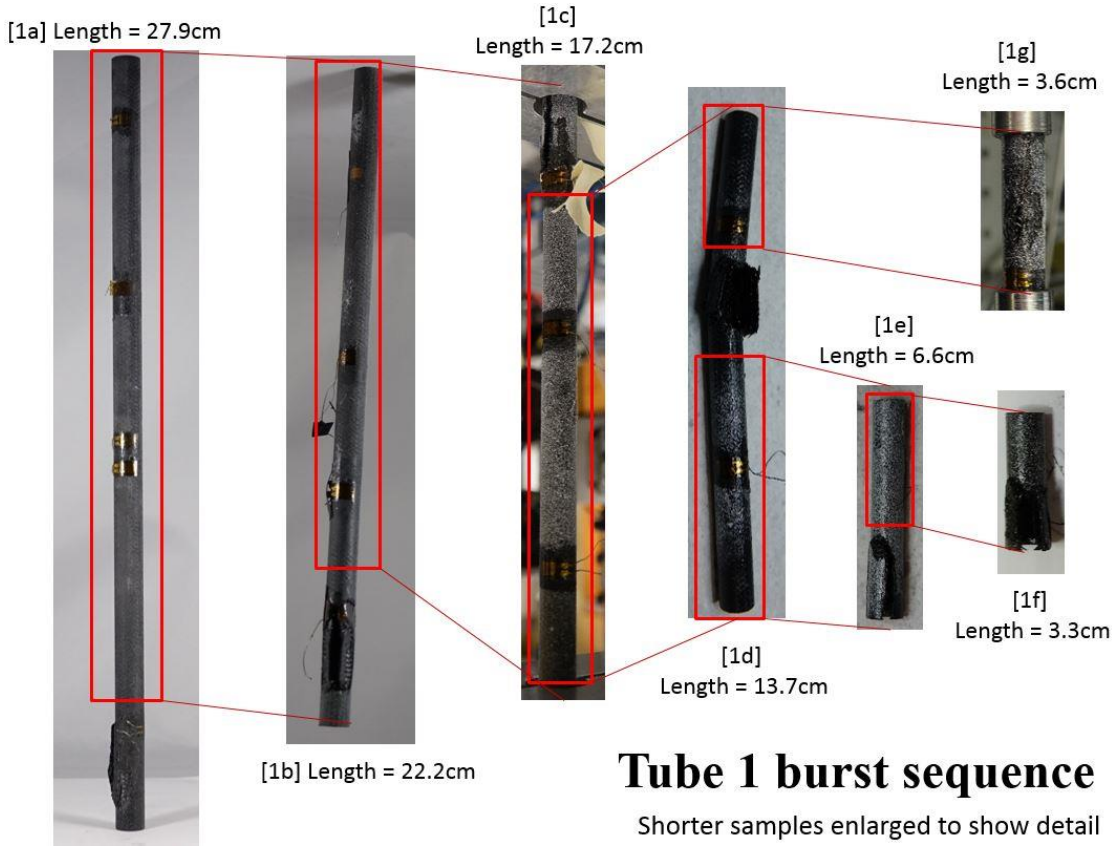

Figure 3.6: Tube 1 burst sequence

Tube 1 was loaded to burst sequentially eight times in tests labelled A-G. Most of the failure modes of the longer specimens were type 1 failures, with types 4, 5, and 6 beginning to occur as samples became shorter. *Figure 3.7* provides the stress/strain and

cumulative AE behavior of Tube 1a, the first test in the series. It is clear from this graph that the behavior of the SiC_f/SiC_m composite tubing follows the behavior observed by Alva. The pressure history in this test terminates at an outer diameter UTS of 99.9 MPa. Compare this value with the similar graph of Tube 1b in *Figure 3.8*, wherein the cumulative AE energy does not reach any considerable value before this point and begins to rise after the stress curve reaches that value. Similar results were taken for the rest of Tube 1 testing, as well as for Tube 2 and Tube 3. This demonstrates the Kaiser effect, as previously discussed, and suggests that the tubes were each properly loaded in a uniform state. A summary of these findings is provided in *Table 3.1*.

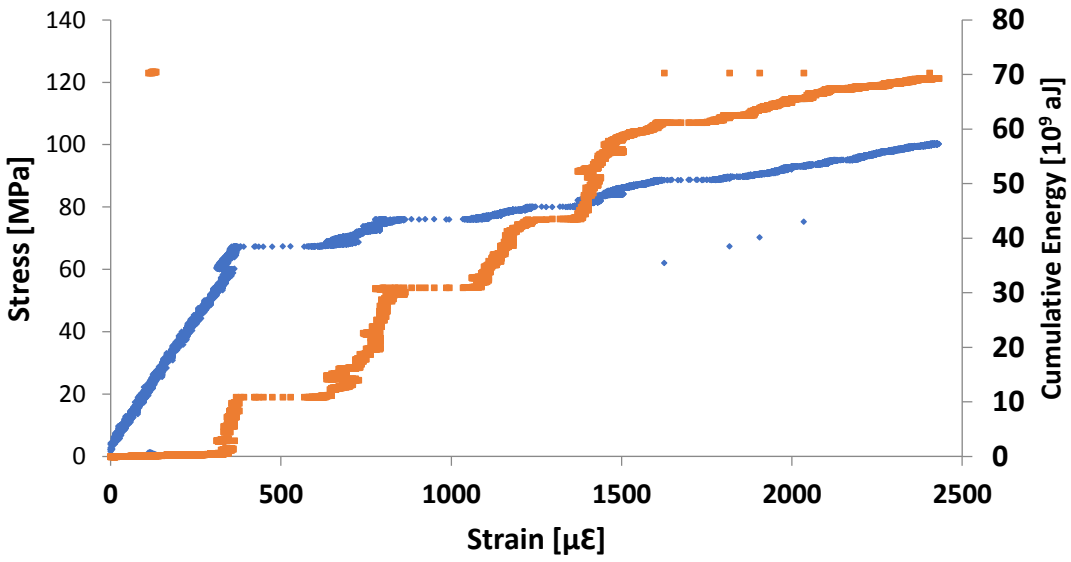

Figure 3.7: Tube 1a Stress/Strain with cumulative AE energy

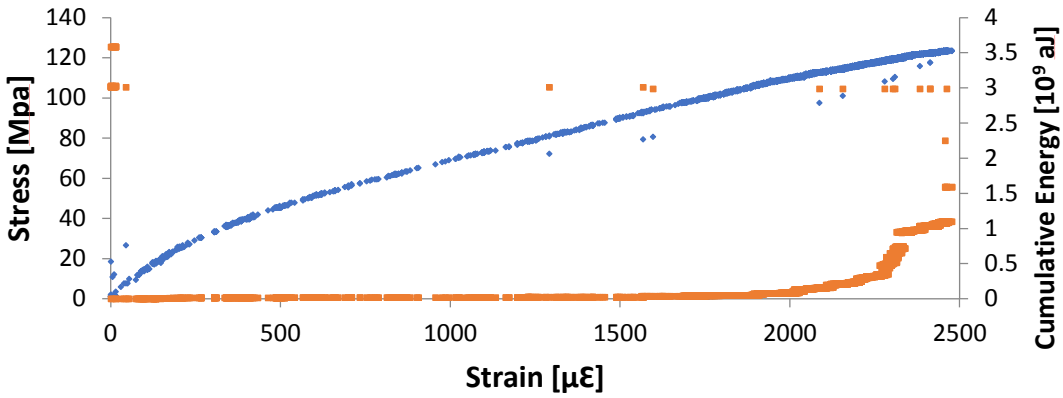

Figure 3.8: Tube 1b Stress/Strain with cumulative AE energy

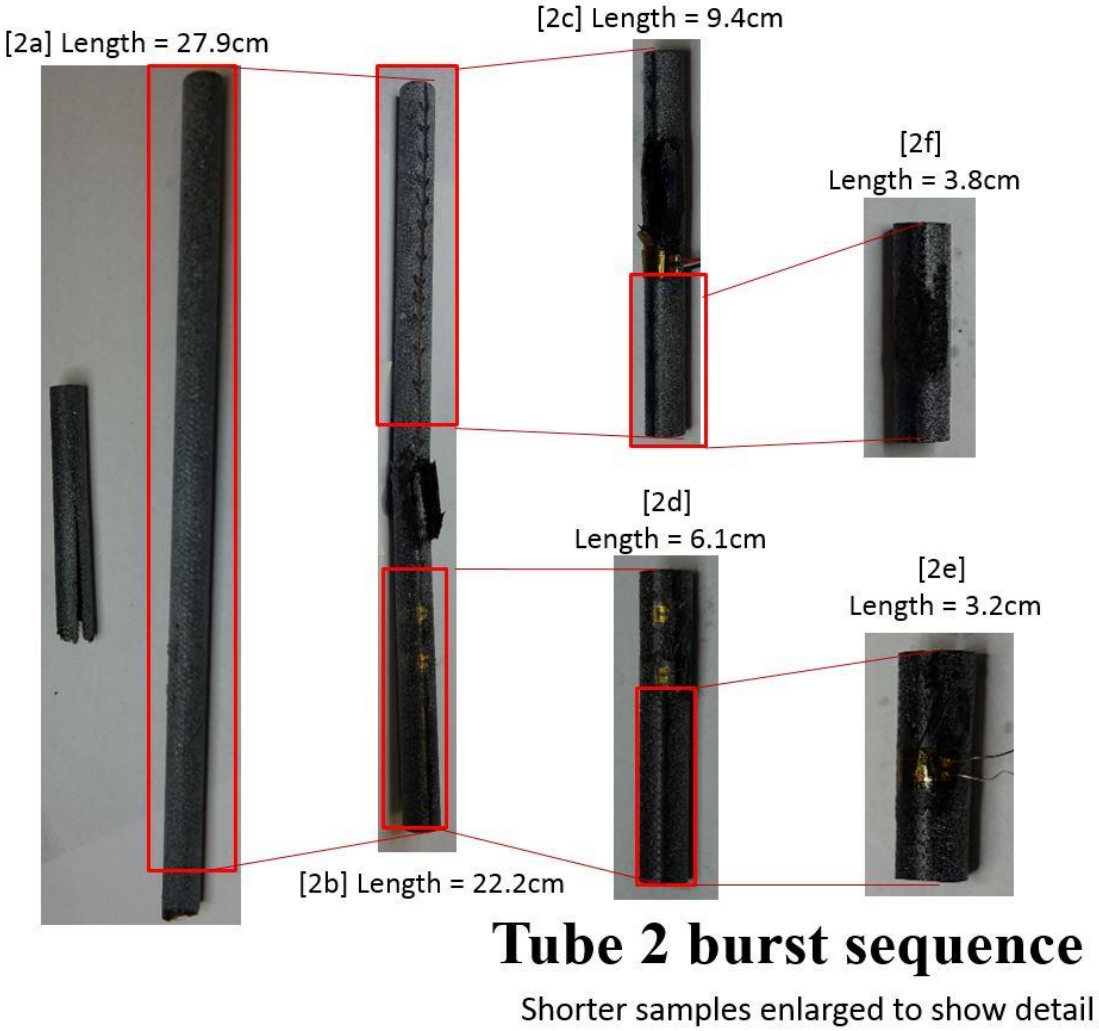

Figure 3.9: Tube 2 burst sequence

Tube 2 yielded six burst tests labelled A-E and exhibited failure types 1, 2, 4, 5, and 6. This sequential burst test yielded typically higher than average outer diameter UTS results compared with the other samples. Tube 3 yielded only four samples labelled A-D due to longer crack lengths and proximity to the edge for each crack. The failure mode of each specimen only consisted of type 1 failures, with the first failure being noticeably longer than the other three. Outer diameter UTS results by tube length for this sample were average compared to the other two tubes.

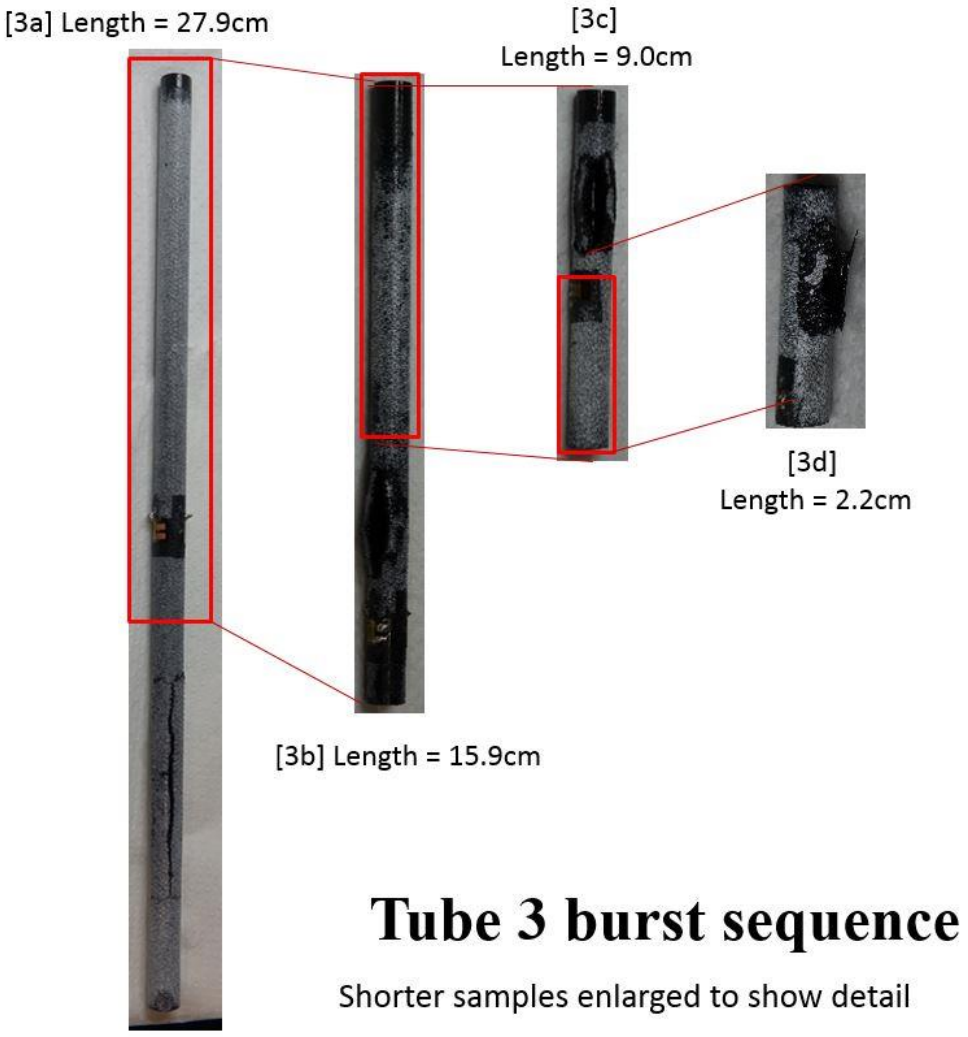

Figure 3.10: Tube 3 burst sequence

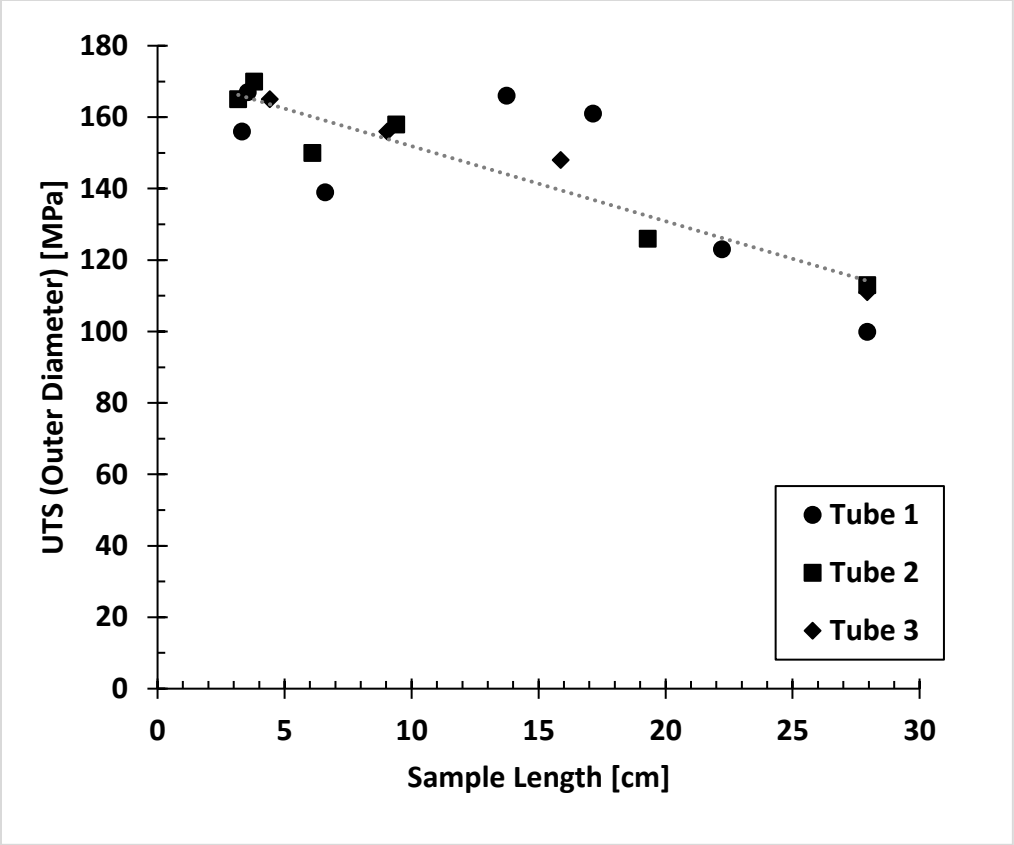

Figure 3.11: Summary of UTS by sample length for all tests

Table 3.1 and *Figure 3.11* show the results of this investigation. It is shown that as each sample is burst and cut in a sequential order that the outer diameter UTS of the sample rises. All three tubes began at similar lengths with UTS in the range of 99-113 MPa and ended at much shorter lengths with outer diameter UTS results clustered in the range of 155-170 MPa. Strength increases appear to begin immediately after testing begins and reach a steady condition near 16cm lengths. Following this point, the trend dips down slightly due to edge breaks in tubes 1e and 2d before rising back up to the steady condition.

Table 3.1: Summary of Burst Test Results

Sample	Length [cm]	Outer Diameter Burst Strength [MPa]	Failure Mode Type
1a	27.94	99.9	1
1b	22.22	123	1
1c	17.14	161	6
1d	13.74	166	1
1e	6.60	139	5
1f	3.32	156	4
1g	3.56	167	5
2a	27.94	113	2
2b	19.30	126	1
2c	9.40	158	1
2d	6.10	150	4
2e	3.17	165	5
2f	3.81	170	6
3a	27.94	111	1
3b	15.88	148	1
3c	9.04	156	1
3d	4.42	165	1

3.6 CONCLUSIONS

There is a clear trend between sample length and outer diameter UTS in these samples, as the sectioned tubes gain as much as 33% additional ultimate strength compared

to the original samples, suggesting the presence of a considerable size effect in this material, though it is difficult to quantify the presence of such defects in numeration and severity through these results alone. In order to perform that analysis, it would be necessary to quantify the type, extent, and number of defects in a set of specimens using several NDE methods and then attempt to link them to UTS. However, this would be greatly complicated by the unpredictable failure progression within such complex structures. In any case, it is likely that the upper limits of UTS found in these tests are more representative of the material strength in the absence of critical defects. Further optimization of manufacturing processes related to this material geometry could improve the ultimate tensile hoop strength to the order of 170 MPa, and as optimal fiber architecture and matrix infiltration methods are studied the strength of SiC_f/SiC_m composite claddings should surpass the values found in this investigation.

However, it is important to note that this data set is limited to three samples manufactured in similar conditions, and that these results may be directly caused by errors in manufacturing or other anomalies. This is supported by the fact that this material shows a large underperformance compared to previously tested materials [51]. As stated previously, results from several other studies [58,59] do not show such a size effect within SiC_f/SiC_m materials. Therefore, it is necessary to posit that the results presented here may be an anomaly and that additional testing with larger sample sizes, higher quality manufacturing, and longer starting geometries is necessary to determine whether this phenomenon really exists in SiC_f/SiC_m cladding geometries.

Another important piece of information related to these results is the propagation of fiber failure in the specimens. Most samples tested showed type 4 fully arrested fiber

crack propagations that only allowed failure to progress a distance on the order of 25mm. While this passes the failure criteria for nuclear fuel cladding (in fact, microcracks beginning at PLS are cited as the initial failure criteria), it demonstrates one of the failure-tolerant strengths of SiC_f/SiC_m composites. As previously mentioned, localized failure to small area of the structure is a desirable quality of this material. In the event of an accident, these composite tubes have a high likelihood of small local failure. Compared to traditional Zr cladding, this would seem to indicate that SiC_f/SiC_m tubing under burst failure behaves comparatively better, since Zr cladding can develop very long, catastrophic breaks in the event of a brittle failure or otherwise exhibits large deformation ballooning in ductile failures [62].

CHAPTER 4

NOVEL OPTICAL SETUPS FOR 2D/3D DIGITAL IMAGE CORRELATION

4.1 DIGITAL IMAGE CORRELATION

Digital image correlation has been used to measure mechanical strain since 1985 [20]. Originally, this method used a single camera to view a speckle pattern applied to the surface of the object under consideration. When the object is loaded, the camera takes a series of images of the speckle pattern which deforms at the same rate as the surface of the material. When the test (or some mechanical function) is complete, these images are analyzed with a digital image correlation software to convert the movement of the speckle pattern into strain maps of the mechanical object. While some similar methods that could accomplish this goal had matured prior to this discovery, they were limited to use under specific laboratory conditions and required intense data processing. Digital image correlation overcame these problems by allowing the full field strain measurement of a surface with a camera, speckle pattern, and adequate lighting. Furthermore, the use of continuum mechanics provided the foundation upon which efficient software could be used to process the results. Since that time, this digital image correlation method to measure translation and rotation in one plane perpendicular to the axis of the camera at a fixed distance has been more specifically termed ‘2D DIC,’ and has enjoyed widespread use in research and industry [63].

An important step forward with this technology was the addition of a second camera which enables both in-plane and out-of-plane motion of the speckle pattern [64]. This stereo or 3D DIC method was able to remove the limitation of a flat surface and allow the measurement of arbitrarily curved surfaces such as airplane wings [65], satellite antennae [66] and cylindrical objectives [67]. This innovation effectively moved the DIC technology from validation of expected in-plane strain of simple objects to analysis of the behavior of complex isotropic structures. As a result, the 3D DIC measurement of design prototypes have made far-reaching contributions to the design philosophy and implementation of a wide variety of products [68].

In the context of SiC_f/SiC_m composite claddings, the benefits provided by DIC strain measurement are essential for several reasons. First, while DIC is already used to great effect at measuring the mechanical response of complex isotropic structures, it is important to note that the use of strain gauges can also adequately measure much of the strain response with lower error and without missing key changes in different regions of the material. The same cannot be said for composite materials, where sharp changes in the strain response can be present in unpredictable locations and regions of the material. While strain gauges can provide an adequate representation of the overall strain and strain behavior exhibited by the material, they fail to capture key differences in strain behavior that arises from the inhomogeneity of the composite material [69]. This is extremely important for understanding the role that the matrix, fibers, and matrix-fiber interface plays in determining the mechanical behavior of the material. Also, the ability to measure out-of-plane motion provided by 3D DIC is critical for the strain measurement of tubular composite nuclear fuel cladding. Several studies have already outlined the use and

effectiveness of using 3D DIC to produce strain maps of the surface of braided CVI SiC_f/SiC_m composite claddings [70,71,72]. These measurements are useful in providing a comprehensive analysis of the surface strain on the specimen, quantifying the strain, and corroborating readings from strain gauges.

4.2 THE TRADITIONAL 2D AND 3D APPARATUS

The most basic DIC setup is that of a single camera pointed at a speckled objective. Bright, uniform white light is typically used to illuminate the flat objective, which is faced perpendicular to the axis of the camera. The camera is connected to a computer which records images from the camera at a set capture rate. A separate program on the computer is used to process the images and compute the strain map. The distance between the sample and the camera must be fixed.

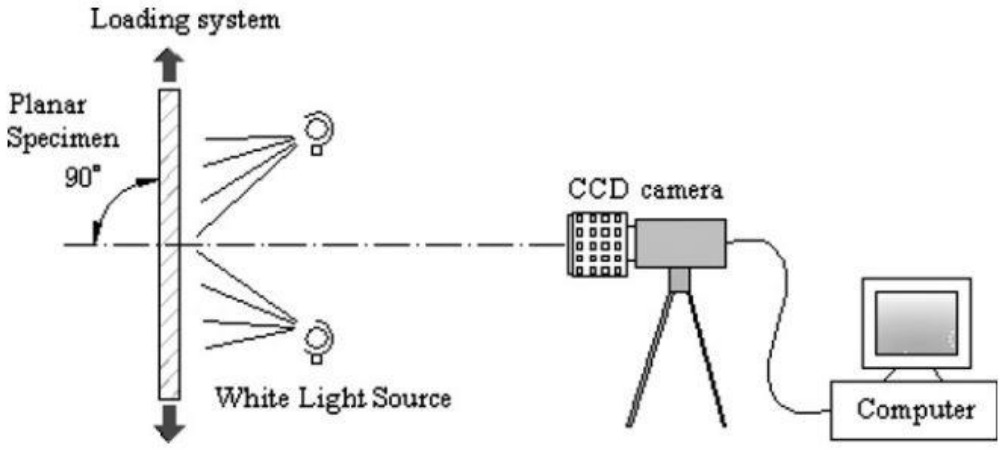

Figure 4.1: 2D DIC Setup diagram [63]

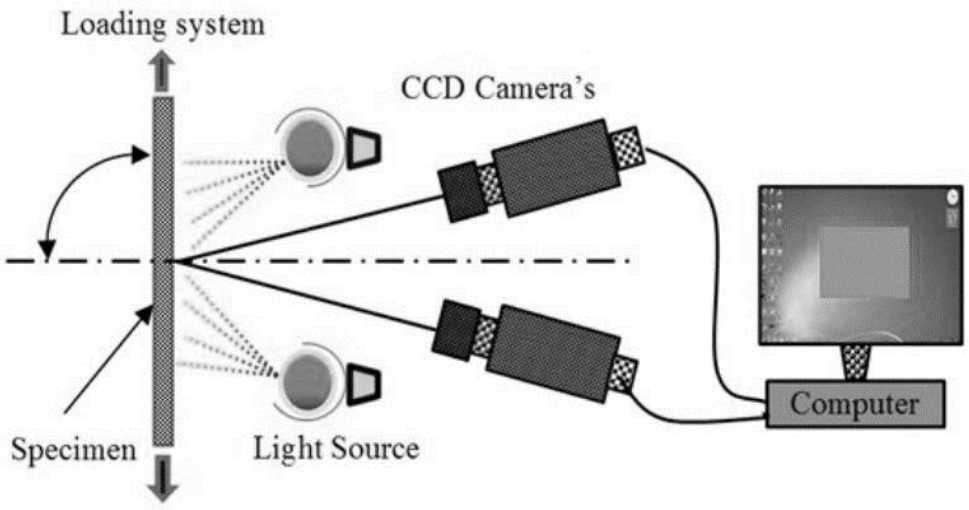

Figure 4.2: 3D DIC Setup diagram [73]

The 3D DIC apparatus is very similar to that of the 2D DIC, except that there is a second camera and the calibration process is quite a bit more vigorous. Typically, the cameras are arranged at a fixed angle, typically 15˚. This angle provides enough separation so as to allow for the deduction of out of plane motion and curvature of the specimen while leaving enough similarity for the software to lock on to the speckle pattern in both views. To achieve calibration in 2D DIC, a known distance in the image is required (such as a ruler or item of known length) and the calibration can be done using software. For 3D DIC, a calibration target is required, and a series of images of this target must be taken. During this process, the target must be translated, tilted, and rotated in small increments so that the software can compute the differences between the views. This calibration yields differences in the angle, pitch and yaw of both cameras relative to one another.

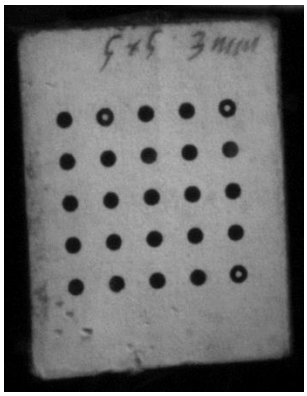

Figure 4.3: 3D DIC Target

4.3 SINGLE CAMERA 3D DIC USING MIRROR SPLITTING TECHNIQUE

Yu & Pan [74] investigated the practical use of a stereo 3D DIC setup using only one camera and a mirror assembly. Prior to this work, there had not been many studies related to the validation of such a setup in the context of work with DIC. The setup itself was a simple centered four-mirror approach like that in *Figure 4.4* (e).: A set of mirrors which lie symmetrically about the camera axis accept light coming from the sample and redirect it towards the camera. The positioning of the mirrors creates the effect of two "virtual" cameras in line with the path of light between the sample and first set of mirrors. When viewed from the perspective of the camera, this splits the view into two halves, each containing a view of the sample.

There are many benefits to using such a system. The first is that the cost of the system is reduced. DIC systems often utilize expensive high-speed cameras or require multiple configurations of DIC cameras which are used to surround a sample geometry (such as a composite tube). It should also be pointed out that while a second camera is not

being used, the sensor coverage of the camera in use is effectively doubled. The second advantage is that while a traditional system requires the adjustment of both cameras to provide a clear view of the sample, this system only requires an adjustment of the mirrors and the camera lens, which can be more advantageous. Yu & Pan also point out that this provides an advantage over view-splitting techniques such as bi-prisms or diffraction gratings in that much larger samples can be tested. Another advantage is that the elimination of a second camera increases the available bandwidth when saving images to the computer. On a system which ran one image capturing device using the traditional system, two systems could be run using this new approach. Also, because camera sensor sensitivity can vary between different cameras of the same make and model, using the same sensor to acquire both views can in theory provide a benefit to the accuracy of the system.

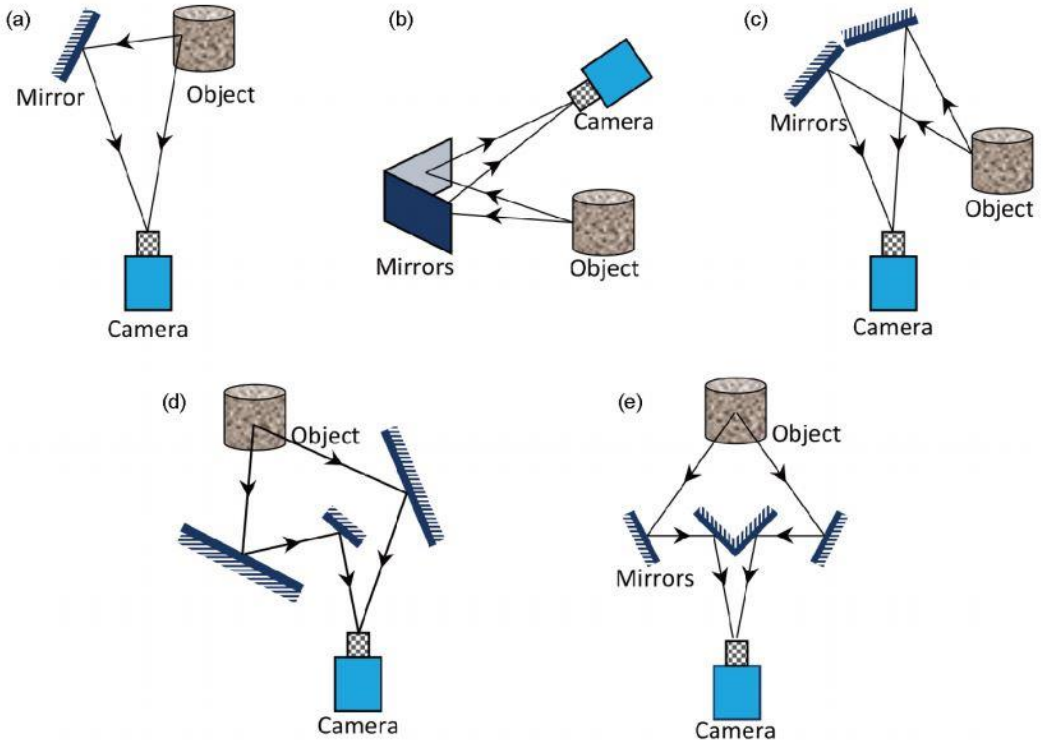

Figure 4.4: Various mirror splitting setups discussed by Bing et. al [75]

While Yu & Pan made the original contribution in this area by validating the concept, their setup was never meant for extensive use in the lab and was only made as a temporary setup. In this work, a stereo DIC setup using this mirror configuration is presented that was designed and fabricated for practical, portable use in the research of the mechanical behavior of SiC_f/SiC_m composites. This setup was validated using curvature analysis, zero strain, and by strain analysis of an aluminum tube subject to uniform internal pressure loading. The strain results of the aluminum tube were compared with readings from a strain gauge as well as results from a traditional DIC setup from a test run under identical conditions.

Several design criteria needed to be met for the creation of a practical stereo DIC mirror assembly such as this. First, the design must be compact and portable, with the mirror assembly fixed relative to the camera at all times, either in use or in transportation. Next, the mirror assembly used needed to provide equidistant pathing of light from the sample to the camera while maintaining a 15˚ separation between views of the sample. Also, the setup needed to be well protected in the event of failure of the specimen. In a failure scenario such as burst of a SiC_f/SiC_m composite tube, fragments can be accelerated to high velocity which can damage or destroy the expensive optical equipment being used, such as the mirrors or the camera lens. Also, the completed design required validation for use in the lab. Finally, a way to digitally segment the images collected by the camera in order to provide the two views was necessary.

To solve these problems, the mirror configuration used by Yu & Pan was replicated because of its symmetry and compact nature, and the final product is shown in *Figure 4.5*. The mirrors used were first surface mirrors which would not add distortion from a layer of

glass between the mirror and the light path. The angles and position of each mirror were designed and mounted to a rigid steel plate via optical clamps. This plate was attached to an 8020 sliding/locking mechanism to provide ease of access to test fixtures as well as to provide simple adjustment of focus. On top of the plate, four optical holders were mounted and a locking clamp was applied to maintain the angles between each holder. Mirrors were then placed on the optical holders. Behind the mirror assembly a rigid block was added to provide a mount for a FLIR Grasshopper 3 9.1MP camera as well as to elevate the position of the camera. An Edmund Optics 50mm fixed focal length C-mount lens was applied to the front of the camera. At the front of the device, a mount was added for a rigid sheet of optical acrylic in order to shield the device from debris while having a negligible effect on the optical path of light coming from the specimen. Lighting is produced separate from the single camera stereo DIC assembly, though an adapter was fashioned to allow the use of a bandpass filter with the setup. To segment the images, a python script was developed to split each image captured by the camera into two halves, each halve being saved and named according to the virtual camera (0 or 1) it belonged to. The completed rig is featured in *Figure 4.5*.

Validation of this system consisted of using Vic-3D for computation of sample curvature for the purposes of computing diameter, analysis of zero strain as well as a loading test on a 6061-aluminum sample, compared to the measurement given by a traditional two camera system using similar cameras and lenses. A strain gauge was attached to the aluminum sample to provide strain measurement as a reference to gauge the accuracy of both of the setups. The pressure loading mechanism used for this was similar to the one discussed in Chapter 3.

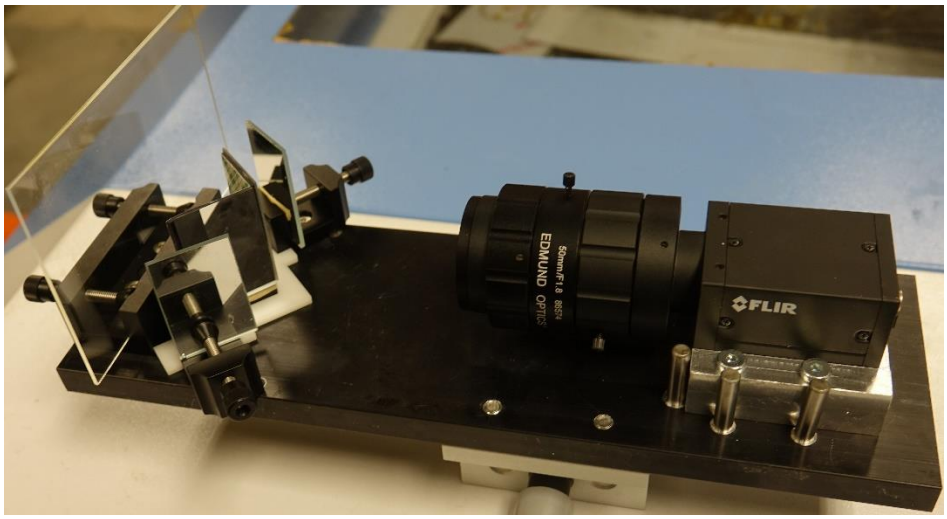

Figure 4.5: One camera 3D DIC rig using mirror splitting technique

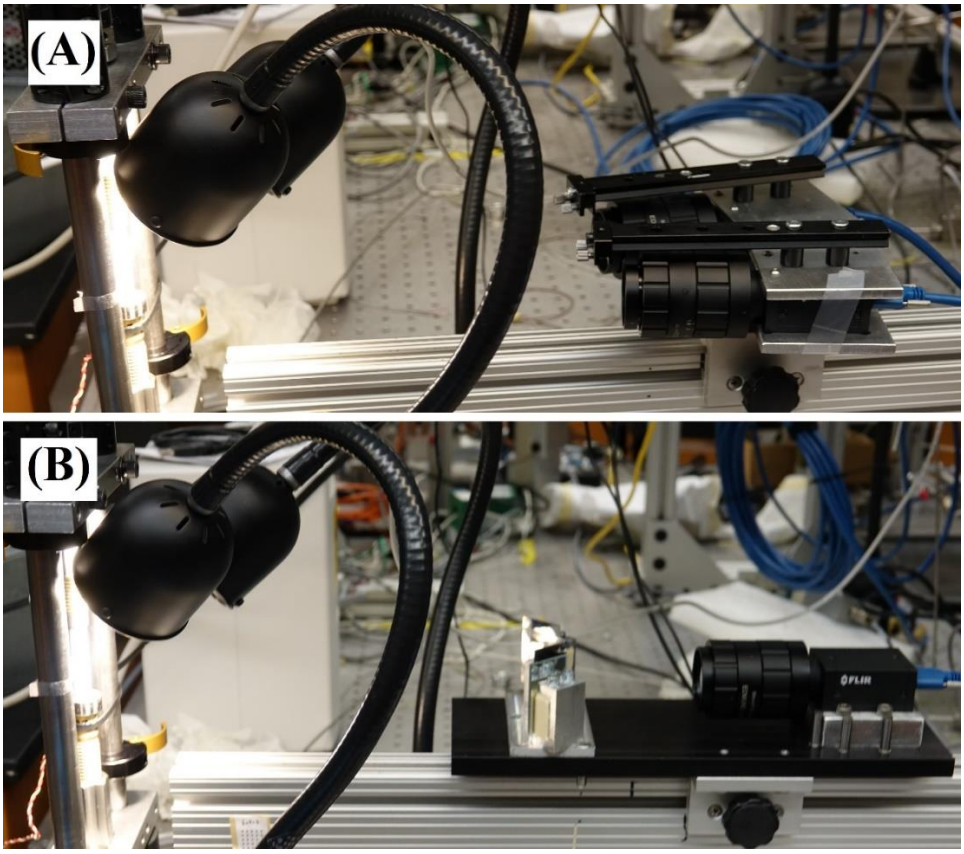

Figure 4.6: Visual test comparison of (A) two-camera 3D DIC system and (B) one-camera 3D DIC system with mirror splitting

The images were processed using the Vic-3D program. Vic-3D separates the results of a test into the following strain modes: E_1, E_2, E_{xx}, E_{yy}, and E_{xy}. E_1 and E_2 represent the

principal strains present in the area of interest while E_{xx}, E_{yy}, and E_{xy} represent the strain in the X-direction, Y-direction, and shear (XY) direction respectively, wherein the X and Y directions are decided by the orientation of the camera(s). In the case of these trials, the first principal strain E_1 was decided to best represent hoop strain on the sample because it corrects for any tilt or misalignment of the sample relative to the camera(s). In the case of the loading trial, E_1 was compared to the E_{xx} value and was found to more closely follow the strain curve represented by the strain gauge.

Vic-3D is used to calculate sample curvature as well as to estimate sample diameter. In all trials, as much of the sample as was in view was used for these calculations, with the exception of the high error regions located on the edges of the aluminum tube. *Table 4.1* yields the results of the performance of each camera system in determining the diameter of the aluminum tube, compared with a measurement taken using calipers. The measurement taken with calipers was performed six times in various locations of the tube and then averaged. The results indicate that while the one camera system estimates within 10% of the expected value, it underestimates the curvature far more than the traditional two camera system.

Table 4.1: Diameter estimation results

Measurement System	Diameter (mm)	Error (%)
Calipers	9.80	N/A
Two-Camera	9.74	0.61
One Camera	9.27	5.41

Next, a zero-strain analysis of the sample was conducted by allowing the sample to remain unloaded throughout the duration of a 20-second test. The principal strain was computed with Vic-3D and the results were compared using the standard deviation from zero. The resulting readings are provided in *Figure 4.7*, and while the one camera system underperforms compared to that of the two-camera system, the performance is comparable.

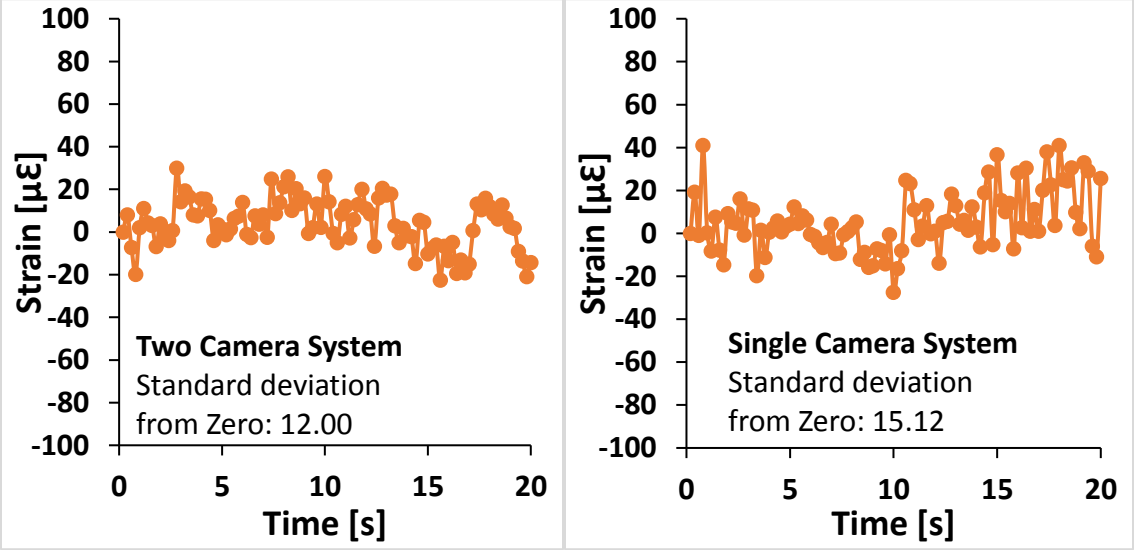

Figure 4.7: Computed E_1 zero strain results of (left) two camera system and (right) One camera system with mirror splitting.

The last validation trial performed was a set of loading tests on the aluminum sample in which strain was induced for the purpose of measurement by the DIC systems. In each case, the sample was loaded to 2ksi yielding a hoop strain of approximately 500με as indicated by the strain gauge. Once the desired strain was achieved, the pressure was held constant and DIC measurement was performed. The results were compared visually as given in *Figure 4.8* as well as by computation of the standard deviation of E1 from the strain curve at the end of the test.

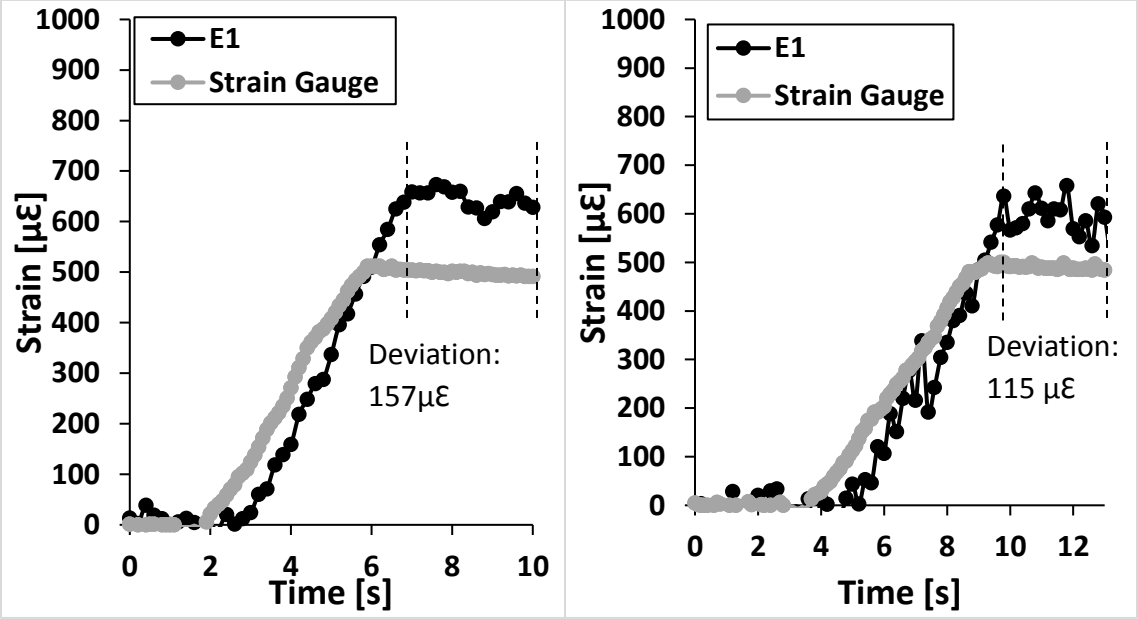

Figure 4.8: Loading test results of (left) two camera system and (right) one camera system with mirror splitting

While both of the camera systems presented an error of the greater than 100με towards the end of the loading scheme, the two-camera system behaved somewhat better according to the standard deviation from the results of the strain gauge. That said, the two-camera system appears to provide a more precise reading than the mirror splitting system, especially during the strain change as the sample is loaded.

Error in the single camera system is likely highly dependent on the quality and status of the mirrors used in the assembly, and care must be taken to eliminate dust and oil from the mirrors and protective shield before running tests. While this system appears to underperform in certain regards to the two-camera system, it is easy to conclude that the performance differences between the two systems are negligible compared to the host of benefits that the mirror splitting system offers.

4.4 SINGLE CAMERA 2D DIC USING A 360° CIRCUMFERENTIAL VIEW

In this section, an experimental design for capturing four quadrants surrounding a cylindrical objective is discussed. Under load, a composite cladding material may show dramatic differences in the strain map which is unpredictable for viewing with traditional DIC setups, due to the fact that only approximately 40% the circumference of a typical cladding geometry is in view of a typical DIC system. This presents a challenge to those who wish to capture DIC of pre-failure behavior of SiC_f/SiC_m composite claddings in the region of failure. This information can be critical for understanding the exact nature of the damage leading to failure in that region and provide clues for designers to engineer better SiC_f/SiC_m claddings. An example of the nonuniform strain of composite samples is provided in *Figure 4.9*. Note how in this sample a line of high hoop strain appears axially along the sample and forks on the right-hand side.

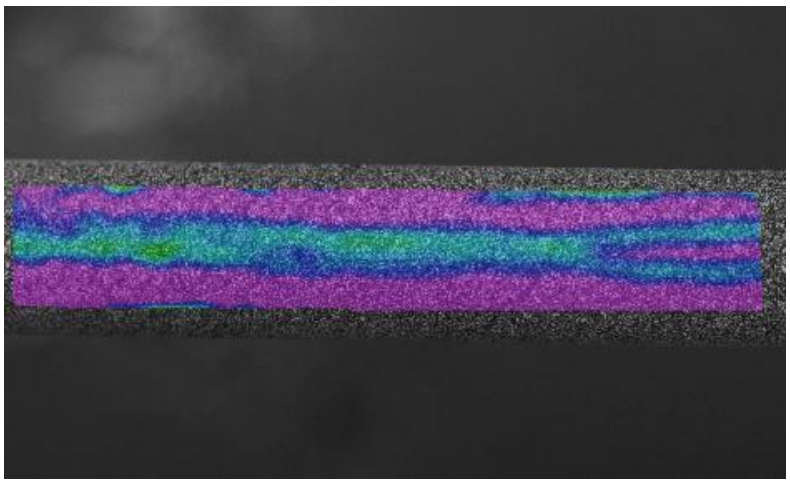

Figure 4.9: (Color) DIC of SiC_f/SiC_m composite tube under internal pressure loading. Green area shows locations of high hoop strain

One way to achieve a full circumferential view is to simply use multiple systems to capture the behavior of the specimen. It is simple to deduce that three of such systems would be necessary to provide a full strain map of the sample. However, this is an expensive approach. A traditional setup like this would require as many as six cameras, or three using the mirror splitting technique described in the previous section. Furthermore, the cost of this process is complicated by the additional hardware necessary for mounting the systems and computers to record the images. More complications arise when contemplating the synchronization necessary, and the sheer complexity of building a test rig that provides adequate space for the multiple DIC systems as well as providing them with a clear view of the target.

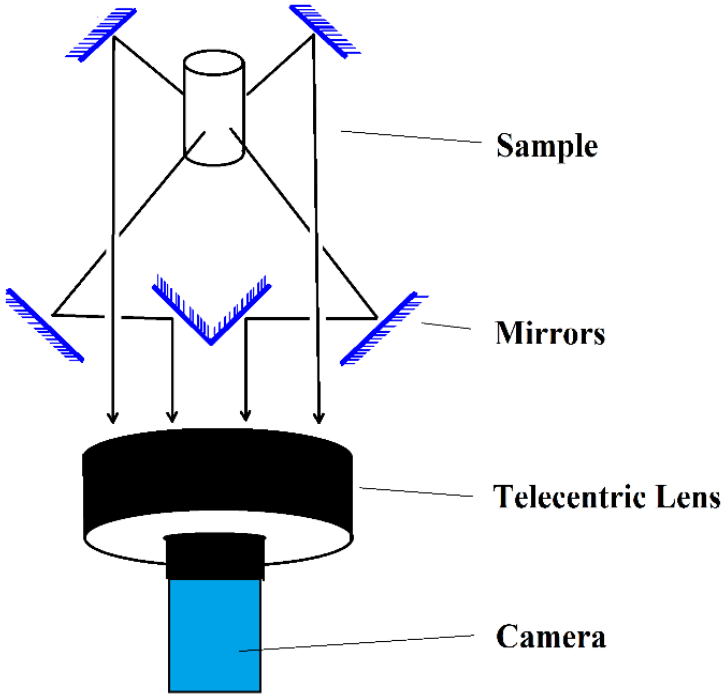

Figure 4.10: Diagram of mirror layout for "hall of mirrors"

In this discussion, an alternative to increasing the number of cameras used was evaluated. In the spirit of the work performed by Yu & Pan, a system of six mirrors were designed to direct light from each of four views to a telecentric lens connected to a single camera. Each mirror was mounted in order to provide a view of a different quadrant of the sample and provide a 360˚ overview of the strain map surrounding the circumference of the specimen for the purpose of using 2D DIC to capture strain on the surface. A basic diagram of such a mirror assembly, referred to here as the "hall of mirrors," is presented in *Figure 4.10*.

To make this design practical, the mirror arrangement was kept in a compact assembly that would be able to slide in and out of an existing test rig. In order to get all of the mirrors in view, a large telecentric lens (Edmund Optics TitanTL) was mounted behind the mirror assembly, and the camera (Grasshopper3 9MP 1" CCD) mounted to the back of the lens. All of these components were fitted together on a rigid aluminum bar, with a sliding mechanism under the mirror assembly which allowed it to move in and out of the specimen test area for cleaning and ease of access. *Figures 4.11* and *4.12* provide views of the design and final product.

To test this design, an aluminum sample was loaded to a preset pressure and 2D DIC results from the rig were compared with a theoretical value calculated from Lame's thick wall pressure vessel equations discussed in Chapter 3, based on the known pressure and dimensions of the aluminum tube. The results from DIC were then laboriously processed in order to provide a circumferential distribution of strain based on a global radial coordinate.

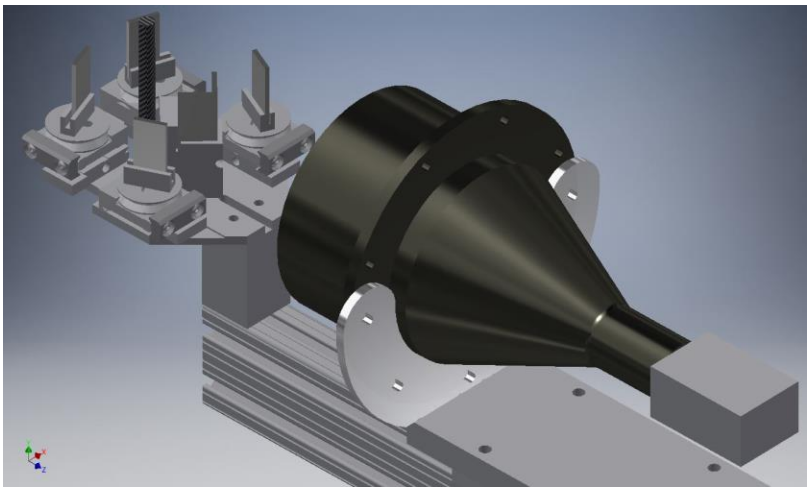

Figure 4.11: CAD design of "hall of mirrors"

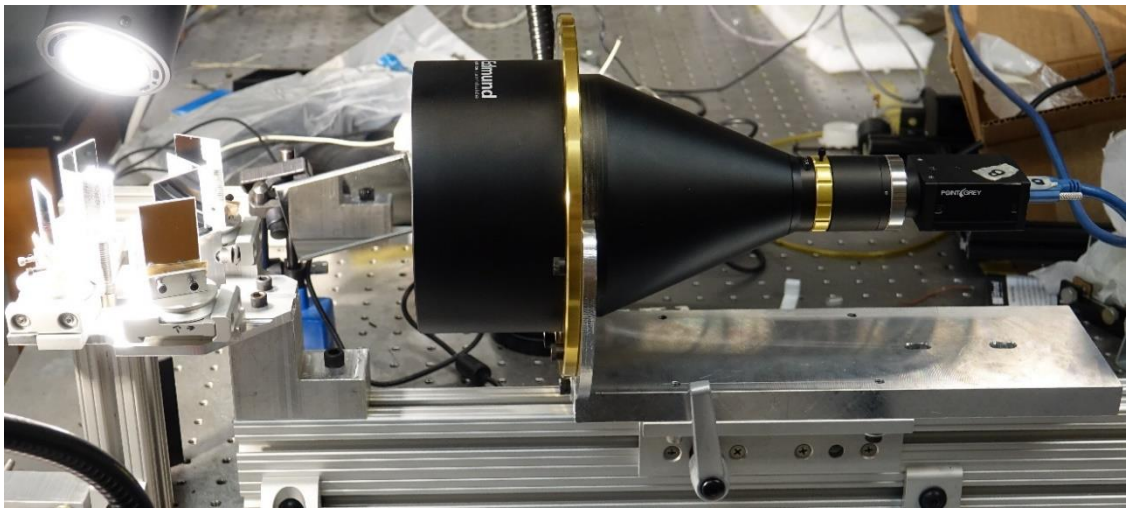

Figure 4.12: Assembled hall of mirrors fixture

To achieve this, a two-part plastic sleeve fitting around the outside of the sample was 3D printed with a series of markings to denote 15˚ increments. A marker was used to place dots on four locations around the sleeve to denote the quadrant or view. When observed from the camera, each mirror was aligned so that the center of each quadrant was centered in the mirror view. *Figure 4.13* provides an example of a view of the aluminum tube with the sleeve placed around it.

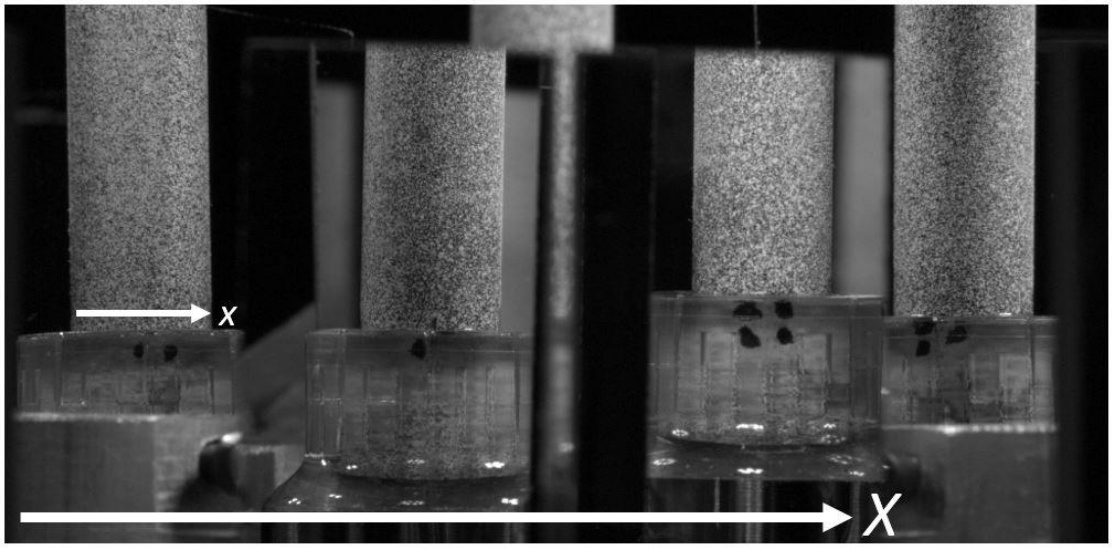

Figure 4.13: Hall of mirrors view including four views of tubular sample and sleeve

After the load test was run on the aluminum tube and the data was acquired, a series of calculations were made to transform the data from each of the four views into a global radial coordinate Θ. To accomplish this, an image was selected and the pixels within the image were used to establish global coordinates *X* and *Y*. The global coordinate *X* was then used to measure the locations of the left and right edges of each view. Then, *X* and *Y* were converted for each view into local coordinates *x* and *y*. Because the telecentric lens produces a two-dimensional transformation of the three-dimensional objective, it was assumed that the coordinates of the left and right edges of each view, x_a and x_b, were a valid indication of the diameter of the sample. Knowing this diameter and the subsequent radius *R*, *Equation 7* was used to transform the local cartesian coordinate system into a local radial coordinate system θ spanning between -90˚ and 90˚.

$$\theta = ASIN\left(\frac{x}{R}\right) \qquad \textit{(Eqn 7)}$$

A diagram showing this transformation is displayed in *Figure 4.14*. Finally, the position of the long markings on the sleeve were used to indicate the center position of the view and establish a local-global shift constant for each pixel in the view, assuming angles of 0˚, 90˚, 180˚, and 270˚, though the center of each view did not always correspond with one of those angles. In each case, a local-global angle shift was calculated and applied to every value. Thus, each pixel value in each view were converted into a global radial coordinate Θ.

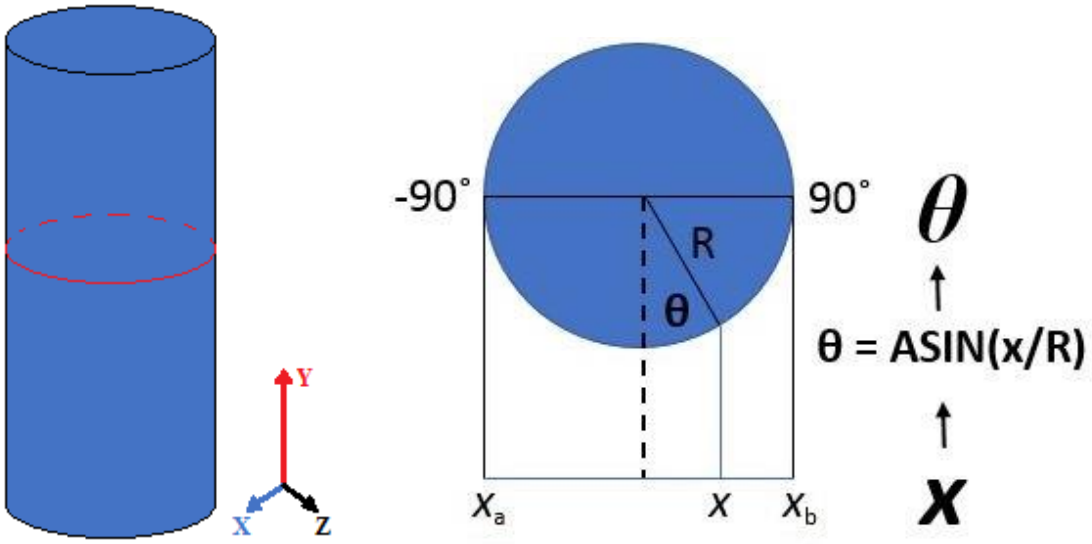

Figure 4.14: (Left) cartesian coordinate system of cylinder with red outline to mark position of horizontal slice. (Right) Diagram of local cartesian coordinate x transformation to local radial coordinate θ. Equation 7 added for clarity.

Using this system, a strain map was built for the sample and a horizontal slice taken from the approximate center of the *Y* coordinate system of the sample was used to provide a circumferential distribution of strain on the sample's surface in the final stage of the test during which the sample was kept at a known constant load. The position of the horizontal slice is marked in *Figure 4.14*. Vic-2D was used to compute the strain values, which provided the strain in the hoop direction of the sample (x-direction of images) Exx. The

final circumferential distribution is provided in *Figure 4.15* with an indicator to show the expected uniform strain on the sample.

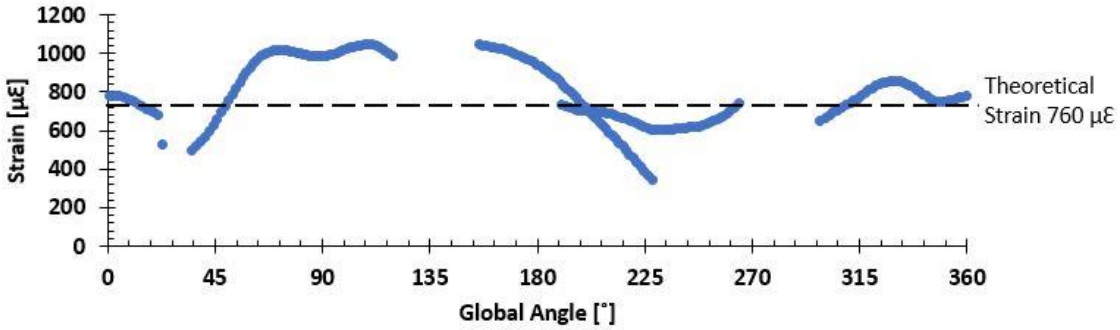

Figure 4.15: Circumferential distribution of strain E_{xx} on the midsection of the trial aluminum tube

The circumferential distribution provides an indicator of the accuracy of the system as well as the system's ability to acquire a strain map of the entire specimen. In this trial, 76.4% of the circumference of the sample was successfully used to compute strain readings using 2D DIC. User error likely caused the views within the region of 180˚ and 225˚ to overlap, and it is expected that a perfect alignment of the mirrors would provide coverage of 84.7%. The distribution is not expected to be able to provide coverage of 100% of the circumference because high distortion in the views caused by the geometry of the cylinder have an undesirable effect on the accuracy of the DIC readings. 2D DIC only works for surfaces perpendicular to the optical axis of the camera. As such, the strain readings on a curved surface computed by Vic-2D were not considered to be very accurate. Error of the readings relative to the expected 760με value were high with a standard deviation of 168.2με from the expected value, though there is a noticeable difference in accuracy between views. Still, the accuracy of the views inhabiting the region between 180˚ and 22˚

seem to be relatively accurate and provide a standard deviation of 87.9με from the expected value. With this setup, a 360-degree view of the sample was obtained. This allows for the capture the failure sites and modes on the cladding tube. At the same time, the area in which an accurate strain map using single camera and 2D DIC techniques was quadrupled.

While more work needs to be done to fully validate this mirror system for use in the lab, they nonetheless demonstrated the concept and showed that it is a very promising way to expand the view of a tubular specimen under load. Future research into assemblies like this would likely solve problems with error in the DIC of the specimen and provide better results. There are a host of issues with a setup like this that must be solved in order for it to be used as a valid testing apparatus. Among these are a laborious data processing regimen which requires a great deal of time investment by the user, error in the DIC readings produced by radial distortion of the tubular objective, and careful alignment of the mirrors to provide a more complete view of the objective. A shield to protect the mirrors and telecentric lens from fragmentation must also be devised.

REFERENCES

[1] Griffith, Andrew. “Accident Tolerant Fuels.” 22 Apr. 2013, US Department of Energy. Lecture. https://www.nrc.gov/reading-rm/doc-collections/commission/slides/2013/20130422/griffith-slides-20130422.pdf (2019)

[2] Terrani, K.A. “Accident tolerant fuel cladding development: Promise, status, and challenges.” Nucl. Mater 501 (2018) 13-30.

[3] Wikipedia contributors. "Fukushima Daiichi nuclear disaster." Wikipedia, The Free Encyclopedia, 4 Jul. 2019. Web. 8 Jul. 2019.

[4] McCaughey, Bill. “Status of DOE’s Accident Tolerant Fuel Program.” Nuclear Regulatory Commission Briefing on Accident Tolerant Fuel. US Department of Energy 12 Apr. 2018. Lecture. https://www.nrc.gov/reading-rm/doc-collections/commission/slides/2018/20180412/mccaughey-04122018-atf.pdf

[5] Powers, D. "Cladding swelling and rupture models for LOCA analysis." (1980).

[6] Baker, Jr., L, & Just, L. Studies Of Metal-Water Reactions At High Temperatures. Iii. Experimental And Theoretical Studies Of The Zirconium-Water Reaction. United States. (1962)

[7] B. A. Pint, K. A. Unocic & K. A. Terrani (2015) Effect of steam on high temperature oxidation behaviour of alumina-forming alloys, Materials at High Temperatures, 32:1-2, 28-35, DOI: 10.1179/0960340914Z.00000000058

[8] B.A. Pint, Performance of FeCrAl for accident-tolerant fuel cladding in high temperature steam, Corros. Rev. 35 (2017) 167-175.

[9] Unocic, K.A., Yamamoto, Y. & Pint, B.A., Effect of Al and Cr content on air and steam oxidation of FeCrAl alloys and commercial APMT alloy, Oxid Met (2017) 87: 431.

[10] P.L. Andresen, R.B. Rebak, E. Dolley, SCC Resistance of Irradiated and Unirradiated High Cr Ferritic Steels, 2014, pp. 9-13. Pap. C2014-3760, Corros. San Antonio, TX.

[11] B.A. Pint, K.A. Terrani, M.P. Brady, T. Cheng, J.R. Keiser, High temperature oxidation of fuel cladding candidate materials in steam-hydrogen environ-ments, J. Nucl. Mater 440 (2013) 420-427.

[12] Pint, B.A. & Unocic, K.A. Steam Oxidation Evaluation of Fe-Cr Alloys for Accident Tolerant Nuclear Fuel Cladding. Oxid Met (2017) 87: 515.

[13] Burns, J.R. Brown, N.R. Neutron cross section sensitivity and uncertainty analysis of candidate accident tolerant fuel concepts. Annals of Nuclear Energy 110 (2017) 1249-1255.

[14] X. Hu, K.A. Terrani, B.D. Wirth, L.L. Snead, Hydrogen permeation in FeCral alloys for LWR cladding application, K. Nucl. Mater 461 (2015) 282-291.

[15] Shapovalov, K. Jacobsen, G.M. Alva, L. Truesdale, N. Deck, C.P. Huang, X. Strength of SiCf-SiCm composite tube under uniaxial and multiaxial loading. Nucl. Mater 500 (2018) 280-294.

[16] Katoh, Y. Ozawa, K. Hinoki, T. Choi, Y. Snead, L.L. Hasegawa, A. Mechanical properties of advanced SiC fiber composites irradiated at very high temperatures. Nucl. Mater 417 (2011) 416-420.

[17] Senatori, Adam. GE Reports. https://s3.amazonaws.com/dsg.files.app.content.prod/gereports/wp-content/uploads/2015/10/27144633/CMCblade.jpg

[18] "Accident Tolerant Fuel." General Atomics & Affiliated Companies. http://www.ga.com/accident-tolerant-fuel (2019)

[19] Katoh, Y. Snead, L.L. Szlufarska, I. Weber, W.J. Radiation effects in SiC for nuclear structural applications. Current Opinion in Solid State and Materials Science 16 (2012) 143-152.

[20] Sutton, M.A. Peters, W.H. Ranson, W.F. Chu, T.C. Applications of Digital-Image-Correlation Techniques to Expiremental Mechanics. Expiremental Mechanics 25 (1985) 232-244.

[21] Inaba M, Hara T, Inoue H. A stereo viewer based on a single camera with view control mechanisms, In: Proceedings of the 1993 IEEE/RSJ international conference on intelligent robotics and systems, vol.3;1993.p.1857–65.

[22] Gyekenyesi, A. Techniques for monitoring damage in ceramic matrix composites. Journal of Intelligent Material Systems and Structures, 25 (2013), 1531–1540.

[23] Unnthorsson R, Jonsson M.T., Runarsson T.P. "NDT Methods for Evaluating Carbon Fiber Composites". University of Iceland. (2004)

[24] Adolfsson, E. Gudmundson, P. Crack initiation and progression in composite laminates subjected to bending and extension. International Journal of Solids and Structures 36 (1999) 3131-3169.

[25] Ramesh, T. "Damage Mechanics of Composite Materials". Texas A&M University. (2012)

[26] Choi, S.R. Foreign Object Damage Phenomenon by Steel Ball Projectiles in a SiC/SiC Ceramic Matrix Composite at Ambient and Elevated Temperatures. American Ceramic Society 91 (2008) 2963-2968

[27] Maire, E. Withers, P.J. Quantitative X-ray tomography. International Materials Reviews 59 (2014) 1-43.

[28] Baste, S. Guerjourma, R.E. Audoin, B. Effect of microcracking on the macroscopic behavior of ceramic matrix composites: Ultrasonic evaluation of anisotropic damage. Mechanics of Materials 14 (1992) 15-31

[29] Truesdale, N. Mechanical Characterization and Non-Destructive Evaluation of SiC_F-SiC_M Composite Tubing with the Impulse Excitation Technique. 2017. (Master's thesis). https://scholarcommons.sc.edu/etd/4279

[30] Roebben, G. Bollen, B. Brebels, A. Van Humbeeck, J. Van der Biest, O. Impulse excitation apparatus to measure resonant frequencies, elastic moduli, and internal friction at room and high temperature. Review of Scientific Instruments 68 (1997) 4511.

[31] Atri, R.R. Ravichandran K.S. Jha, S.K. Elastic properties of in-situ processed Ti–TiB composites measured by impulse excitation of vibration. Materials Science in Engineering 271 (1999) 150-159.

[32] Hu Xunxiang, Ang Caen K., Singh Gyanender P., Katoh Yutai. "Technique Development for Modulus, Microcracking, Hermeticity, and Coating Evaluation Capability for Characterization of SiC/SiC Tubes". Oak Ridge National Laboratory. (2016).

[33] Montalvão, D., Maia, N.M.M. and Ribeiro, A.M.R.. A review of vibration-based structural health monitoring with special emphasis on composite materials. Shock and Vibration Digest 38 (4) (2006), 295 - 324.

[34] Hamey, C.S. Lestari, W. Qiao, P. Song, G. Experimental Damage Identification of Carbon/Epoxy Composite Beams Using Curvature Mode Shapes. Structural Health Monitoring 3(4) (2004) 333-353.

[35] ASTM E1875-13, Standard Test Method for Dynamic Young's Modulus, Shear Modulus, and Poisson's Ratio by Sonic Resonance, ASTM International, West Conshohocken, PA, 2013, www.astm.org

[36] ASTM E1876-15, Standard Test Method for Dynamic Young's Modulus, Shear Modulus, and Poisson's Ratio by Impulse Excitation of Vibration, ASTM International, West Conshohocken, PA, 2015, www.astm.org

[37] Maheri, M.R. Adams, R.D. Modal vibration damping of anisotropic FRP laminates using the Rayleigh--Ritze energy minimization scheme. Journal of Sound and Vibration 259(1) (2003) 17-29.

[38] Timoshenko S., Young D.H, Weaver W. Jr."Vibration Problems in Engineering". John Wiley And Sons. (1974)

[39] ASTM D7136 / D7136M-15, Standard Test Method for Measuring the Damage Resistance of a Fiber-Reinforced Polymer Matrix Composite to a Drop-Weight Impact Event, ASTM International, West Conshohocken, PA, 2015, www.astm.org

[40] Cheon, J. Lee, S. Im, Y. Experimental and numerical study of the impact behavior of SMC plates. Composite Structures 47(1-4) (1999) 551-561.

[41] Sjoblom, P.O. Hartness, J.T. Cordell, T.M. On Low-Velocity impact testing of composite materials. Journal of Composite Materials 22(1) (1988) 30-52.

[42] Kelkar, A.D. Grace, C. Sankar, J. Threshold damage criteria for thin and thick laminates subjected to low velocity impact loads. International Conference on Composites Materials ICCM 11, Paris 1999.

[43] Chircor, M. Dumitrache, R. Dumitrache, C. The Impact Behavior of Composite Materials. 3rd International Conference on Maritime and Naval Science in Engineering, Constantza 2010.

[44] Ando, K. Ikeda, T. Sato, S. Yao, F. and Kobayasi, Y. (1998), A PRELIMINARY STUDY ON CRACK HEALING BEHAVIOUR OF Si_3N_4/SiC COMPOSITE CERAMICS. Fatigue & Fracture of Engineering Materials & Structures, 21: 119-122.

[45] Alva, Luis & Huang, Xinyu & Chen, X & Everatt, C & Jacobsen, George & Back, Christina. (2014). AE crack initiation and propagation detection in high pressure burst testing of SiC_f-SiC_m composite nuclear fuel cladding. International Congress on Advances in Nuclear Power Plants, ICAPP 2014. 3. 2307-2311.

[46] Fabrication and characterization of joined silicon carbide cylindrical components for nuclear applications. Khalifa, H., C. Deck, O. Gutierrez, G. Jacobsen, and C. Back. s.l. : Journal of Nuclear Materials, 2015, Vol. 457, pp. 227-240.

[47] Guenoun, P. (2013) Design Optimization of Advanced PWR SiC/SiC Fuel Cladding for Enhanced Tolerance of Loss of Coolant Conditions. (Master's Thesis.)

[48] Burns, P.C. Ewing, R.C. Navrotsky, A. Nuclear Fuel in a Reactor Accident. Science 335(6073) (2012) 1184-1188.

[49] Ramesh, T. Singh, C.V. Damage and Failure of Composite Materials. Cambridge University Press, 2012.

[50] G.M. Jacobsen, E. Song, Intra-batch quality control analysis using C-ring testing, Unpublished Data, General Atomics (2016).

[51] Jacobsen, G. M.; Chiger, H. GA-A28712: Product Engineering Materials Property Manual: General Atomics Silicon Carbide Cladding; General Atomics Internal Report (2017).

[52] Alva, L. (2018) Monitoring The Progress Of Damage In A SICf-SICm Composite Nuclear Fuel Cladding Under Internal Pressure Using Acoustic Emission. (Doctoral Dissertation).

[53] Lavrov, A. The Kaiser effect in rocks: principles and stress estimation techniques. International Journal of Rock Mechanics and Mining Sciences 40(2) (2003) 151-171.

[54] Williams, J. H., & Lee, S. S. (1978). Acoustic Emission Monitoring of Fiber Composite Materials and Structures. Journal of Composite Materials, 12(4), 348–370.

[55] Waller, J.M.; Saulsberry, R.L.; Andrade, E. Use of acoustic emission to monitor progressive damage accumulation in kevlar® 49 composites. Qunt. Nondestruct. Eval. (QNDE) Kingst. 2009

[56] Nozawa, T. Ozawa, K. Tanigawa, H. Characterization of failure behavior of silicon carbide composites by acoustic emission. Ceramic Materials For Energy Applications II 33(9) (2012).

[57] Wisnom, M.R. Size effects in the testing of Fibre-composite materials. Composites Science and Technology 59(13) (1999) 1937-1957.

[58] Calard, V., Lamon, J. (2002) A probabilistic-statistical approach to the ultimate failure of ceramic-matrix composites—part I: experimental investigation of 2D woven SiC/SiC composites. Composites Science and Technology, 62(3), 385-393.

[59] Nozawa, T., Katoh, Y., & Kohyama, A. (2005) Evaluation of Tensile Properties of SiC/SiC Composites with Miniaturized Specimens. Materials Transactions, 46(3), 543-551.

[60] Shapovalov K. (2016) Mechanical Characterization of SICF-SICM Nuclear Fuel Cladding by a Novel Hydraulic Internal Pressurization Method. (Master's Thesis).

[61] Tan, K. T., Watanabe, N., & Iwahori, Y. (2012). Impact Damage Resistance, Response, and Mechanisms of Laminated Composites Reinforced by Through-Thickness Stitching. International Journal of Damage Mechanics, 21(1), 51–80.

[62] Takehiko N. Toyoshi F. Tomoyuki S & Hideo S (2004) Failure Thresholds of High Burnup BWR Fuel Rods under RIA Conditions, Journal of Nuclear Science and Technology, 41:1, 37-43

[63] Pan, B. Qian, K. Asundi, A. Two-dimensional digital image correlation for in-plane displacement and strain measurement: a review. Measurement Science and Technology 20(6) (2009).

[64] Jeffrey D. Helm, Stephen R. McNeill, Michael A. Sutton, "Improved three-dimensional image correlation for surface displacement measurement," Opt. Eng. 35(7) (1 July 1996)

[65] Li, L. Liang, J. Guo, X. Hu, H. Tang, Z. Full-field wing deformation measurement scheme for in-flight cantilever monoplane based on 3D digital image correlation. Measurement Science and Technology 25(6) (2014).

[66] Pan, B. , Xie, H. , Yang, L. and Wang, Z. (2009), Accurate Measurement of Satellite Antenna Surface Using 3D Digital Image Correlation Technique. Strain, 45: 194-200

[67] Zhenxing Hu, Huimin Xie, Jian Lu, Tao Hua, and Jianguo Zhu, "Study of the performance of different subpixel image correlation methods in 3D digital image correlation," Appl. Opt. 49, 4044-4051 (2010)

[68] Hall, Loura. "Cars and Planes Are Safer Thanks to This Tool Developed for Shuttle." NASA, 27 July 2018, www.nasa.gov/directorates/spacetech/spinoff/Cars_Planes_Safer_Thanks_to_Tool_Developed_for_Shuttle.

[69] Koohbor, B. Mallon, S. Kidane, A. Sutton, M.A. A DIC-based study of in-plane mechanical response and fracture of orthotropic carbon fiber reinforced composite. Composites Part B: Engineering 66 (2014) 388-399.

[70] Rohmer, E. Martin, E. Lorette, C. Mechanical properties of SiC/SiC braided tubes for fuel cladding. Nucl. Mater 453(1-3) (2014) 16-21.

[71] Alva, L.H. Huang, X. Jacobsen, G.M. Back, C.A. High Pressure Burst Testing of SiCf-SiCm Composite Nuclear Fuel Cladding, in: Adv. Opt. Methods Exp. Mech., vol. 3, Springer, 2015, pp. 387-393.

[72] Croom, B.P. Xu, P. Lahoda, E.J. Deck, C.P. Li, X. Quantifying the three-dimensional damage and stress redistribution mechanisms of braided SiC/SiC composites by in situ volumetric digital image correlation. Scripta Materialia 130 (2017) 238-241.

[73] Sarantha, K.M. Harilal, R. Kashfuddoja, M. Ramji, M. Material Characterization of Carbon Fiber Reinforced Polymer Laminate Using Virtual Fields Method. International Conference on Theoretical, Applied, Computational and Experimental Mechanics. (2014).

[74] Yu, L. Pan, B. Single-camera stereo-digital image correlation with a four-mirror adapter: optimized design and validation. Optics and Lasers in Engineering 87 (2016) 120-128.

[75] Pan, B. Yu, L. Zhang, Q. Review of single-camera stereo-digital image correlation techniques for full-field 3D shape and deformation measurement. Science China Technological Sciences 61(1) (2018) 2-20.